Journal of Sound and Vibration 333 (2014) 6996–7018

Contents lists available at ScienceDirect

Journal of Sound and Vibration

journal homepage: www.elsevier.com/locate/jsvi

The fictitious force method for efficient calculation of vibration from a tunnel embedded in a multi-layered half-space

M.F.M. Hussein [a,*], S. François [b], M. Schevenels [c], H.E.M. Hunt [d], J.P. Talbot [d], G. Degrande [b]

[a] Department of Civil and Architectural Engineering, College of Engineering, University of Qatar, P.O. Box 2713, Doha, Qatar
[b] Department of Civil Engineering, KU Leuven, Kasteelpark Arenberg 40, B-3001 Leuven, Belgium
[c] Department of Architecture, KU Leuven, Kasteelpark Arenberg 1, B-3001 Leuven, Belgium
[d] Engineering Department, Cambridge University, Trumpington Street, Cambridge CB2 1PZ, United Kingdom

ARTICLE INFO

Article history:
Received 20 November 2012
Received in revised form
26 June 2014
Accepted 18 July 2014
Handling Editor: H. Ouyang
Available online 28 August 2014

ABSTRACT

This paper presents an extension of the Pipe-in-Pipe (PiP) model for calculating vibrations from underground railways that allows for the incorporation of a multi-layered half-space geometry. The model is based on the assumption that the tunnel displacement is not influenced by the existence of a free surface or ground layers. The displacement at the tunnel–soil interface is calculated using a model of a tunnel embedded in a full space with soil properties corresponding to the soil in contact with the tunnel. Next, a full space model is used to determine the equivalent loads that produce the same displacements at the tunnel–soil interface. The soil displacements are calculated by multiplying these equivalent loads by Green's functions for a layered half-space. The results and the computation time of the proposed model are compared with those of an alternative coupled finite element–boundary element model that accounts for a tunnel embedded in a multi-layered half-space. While the overall response of the multi-layered half-space is well predicted, spatial shifts in the interference patterns are observed that result from the superposition of direct waves and waves reflected on the free surface and layer interfaces. The proposed model is much faster and can be run on a personal computer with much less use of memory. Therefore, it is a promising design tool to predict vibration from underground tunnels and to assess the performance of vibration countermeasures in an early design stage.

1. Introduction

Significant vibration in buildings near underground tunnels is attributed to moving trains. Vibration is generated due to irregularities of wheels and tracks and propagates to nearby buildings where it is perceived as ground-borne vibration in the frequency range 1–80 Hz and ground-borne noise in the frequency range 16–250 Hz. Vibration at higher frequencies is generally attenuated rapidly with distance along the transmission path through the ground [1]. Vibration transmitted to buildings can cause malfunctioning of sensitive equipment and annoyance to inhabitants. The problem is more significant for shallow tunnels in close proximity to foundations of nearby buildings. Underground tunnels pass under commercial and

* Corresponding author.
E-mail address: mhussein@qu.edu.qa (M.F.M. Hussein).

http://dx.doi.org/10.1016/j.jsv.2014.07.020
0022-460X/

residential areas with a wide range of depths below the surface. For example, the average depth of the underground tunnels in London is 24 m with a maximum depth of 67.4 m. Vibration in buildings can be isolated by using vibration countermeasures, such as floating slab tracks and/or base isolation of buildings [2–5].

Modelling of vibration from underground railways is gaining more interest on account of the need for quick tools to design vibration countermeasures for both existing and newly constructed tunnels. There are two popular methods for modelling, discussed in the following paragraphs.

The first approach is the Pipe-in-Pipe (PiP) model [6–8], where the tunnel and the soil are modelled as two concentric pipes. The inner pipe represents the tunnel wall and is modelled using thin shell theory. The outer pipe, with its outer radius being set to infinity, represents an unbounded soil with a cylindrical cavity and is modelled using elastodynamics. The PiP model is computationally efficient, in both running time and memory requirements, on account of the uniformity along and around the tunnel. The disadvantage of the PiP model in its present form is that it only can account for a tunnel embedded in a homogeneous full space. This may not be sufficient for the modelling of realistic situations.

The second approach employs a coupled finite element–boundary element (FE–BE) methodology [9–11]. The tunnel wall is modelled using the FE method while the surrounding soil is modelled using the BE method. The advantage of this method is the possibility of modelling a free surface and a multi-layered ground, and tunnel walls with non-circular geometries. The computational efficiency of this model has been greatly improved in the last few years by taking advantage of a periodic or longitudinally invariant geometry. For periodic structures, a Floquet transform can be used for the computation of the structural response and the radiated wavefield [10–15]. In the case of longitudinally invariant structures, a computationally efficient two-and-a-half-dimensional (2.5D) approach can be applied [9,16–18], where the Fourier transform of the longitudinal coordinate allows to represent the three-dimensional (3D) response of the structure and the radiated wavefield on a two-dimensional (2D) mesh. Even with these recent developments, the coupled FE–BE models require a significant computational effort. Therefore, coupled FE–BE models are useful for research purposes but still computationally too expensive to be used as a design tool.

The PiP model has been validated against the coupled FE–BE model for the case of a tunnel embedded in a full space [13]. A good agreement is achieved between the results of the two models with much more computational efficiency from the PiP model. This has raised the question of whether the PiP model could be used for more realistic situations such as for modelling a tunnel in a multi-layered half-space.

The objective of this paper is to extend the PiP model to allow for the incorporation of a layered half-space geometry. To this end, it is assumed that the tunnel displacement is not influenced by the existence of a free surface or ground layers, i.e. the displacement at the tunnel–soil interface is the same whether there is a free surface and ground layers or not. This approximation is only valid when the free surface and layer interfaces and the tunnel are sufficiently spaced. Another objective of this paper is to investigate the accuracy of the proposed formulation for realistic cases.

Before presenting the methodology of this work, it is worth to point out a model proposed by Grundmann and Müller [19,20], which has some features from the coupled FE–BE model as well as the PiP model. This model calculates vibration from circular and non-circular tunnels in a full space and a half-space. To account for a circular tunnel in a full space, the shell theory or the FE method is used for the tunnel, while the elastic continuum theory is used for the soil. To account for a non-circular tunnel in a full space, the problem domain is divided into two parts by a virtual cylindrical surface that encloses the tunnel wall. The first is the internal part consisting of the tunnel wall and the soil that lies within the virtual cylinder; this part is modelled using the FE method. The second part is the homogeneous infinite space with an internal cylindrical boundary and is modelled using elastic continuum theory. A half-space is modelled by using superposition of two boundary value problems [21,22]: a tunnel embedded in a full space and an elastic half-space.

This paper is organized as follows. Section 2 describes the methodology used in this paper, where a distinction is made between three calculation steps for the calculation of vibrations from a tunnel embedded in a multi-layered half-space. Section 3 presents a numerical study of the performance and accuracy of the proposed model. Five case histories with different soil layering are considered. The results are compared with reference FE–BE calculations.

2. Methodology

In this paper, a model is presented that allows to compute the vibrations from a tunnel embedded in a multi-layered half-space (Fig. 1). The model is based on the assumption that the near field displacement of the tunnel is not influenced by the existence of a free surface or ground layers, in other words, the displacement at the tunnel–soil interface is the same whether there is a free surface and ground layers or not.

The methodology consists of three steps, as outlined in Fig. 2. In a first step (Fig. 2a), the response of a tunnel embedded in a full space due to a vertical point load F_z at the tunnel invert is computed. The assumption that the tunnel is embedded in a full space allows for a fast evaluation of the displacement at the tunnel–soil interface using the PiP model [6–8].

In the second calculation step (Fig. 2b), a model of a full space (without a tunnel) is considered. A number of equivalent loads in the full space, that produce the same displacement at the tunnel–soil interface as computed in the first calculation step, are determined. The computation of these equivalent loads is fast and performed using analytical fundamental solutions for an elastic full space.

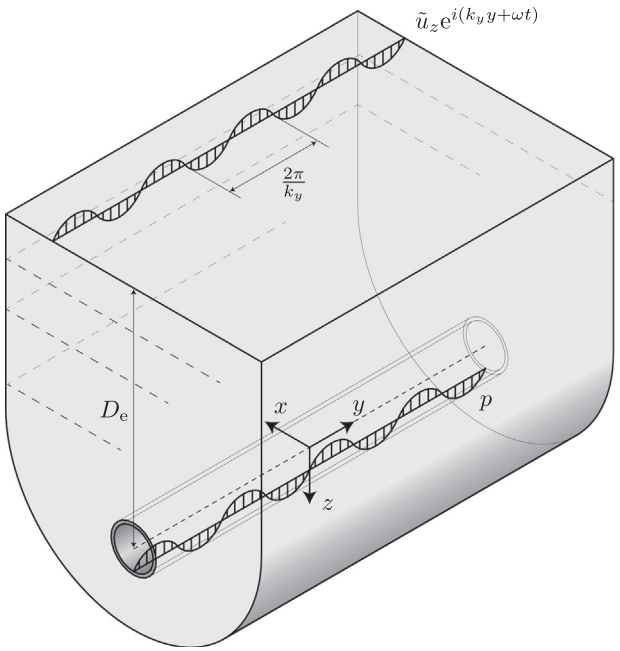

Fig. 1. Tunnel embedded in a multi-layered half-space.

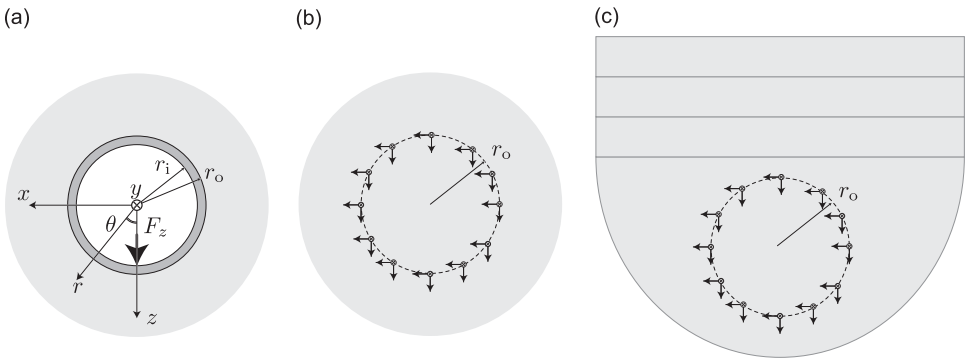

Fig. 2. Proposed methodology: (a) calculation of the displacement at the tunnel–soil interface using a model of a tunnel embedded in a full space, (b) calculation of equivalent loads that produce the same tunnel displacements on the tunnel–soil interface and (c) application of the equivalent loads in a model of a multi-layered half-space.

In the third calculation step, a model of a multi-layered half-space (without a tunnel) is considered. The equivalent loads from step 2 are multiplied by Green's functions of a multi-layered half-space. These Green's functions are evaluated numerically by means of the direct stiffness method [23–25].

The three calculation steps mentioned above are discussed in more detail in the following subsections.

2.1. Step 1: calculating the displacement at the tunnel–soil interface

In the first calculation step, the response of a tunnel embedded in a full space due to a vertical point load F_z at the tunnel invert is computed using the PiP model (Fig. 3). The PiP model is based on a Fourier transformation of the time t to the frequency ω and of the coordinate y along the tunnel axis to the wavenumber k_y. In addition, a Fourier series expansion is employed in the circumferential direction θ.

The 3D displacement in the tunnel and the full space is described by its radial, circumferential and longitudinal components $u_r(r,\theta,y,t)$, $u_\theta(r,\theta,y,t)$, and $u_y(r,\theta,y,t)$ in the cylindrical coordinate system (r,θ,y) (Fig. 1). The Fourier transform of the time t to the frequency domain ω reads as

$$\hat{u}_r(r,\theta,y,\omega) = \int_{-\infty}^{\infty} u_r(r,\theta,y,t) e^{-i\omega t}\, dt \tag{1a}$$

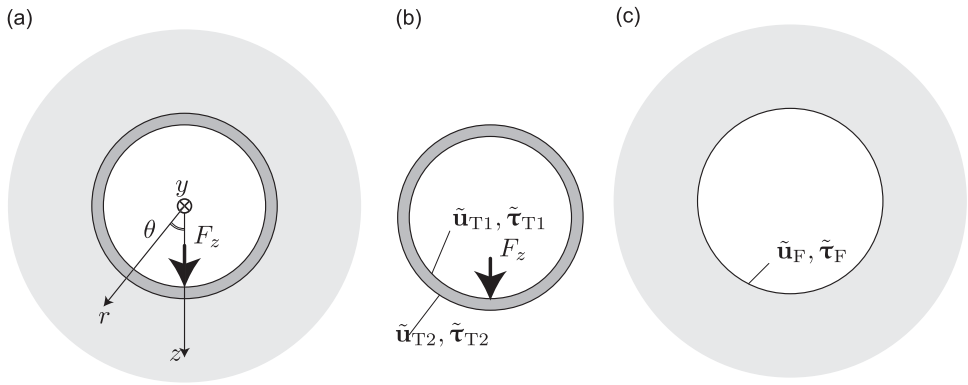

Fig. 3. Calculation step 1: (a) the displacement at the tunnel–soil interface is computed as the dynamic interaction between (b) the tunnel wall and (c) a full space with a cylindrical cavity.

$$\hat{u}_\theta(r,\theta,y,\omega) = \int_{-\infty}^{\infty} u_\theta(r,\theta,y,t)\mathrm{e}^{-\mathrm{i}\omega t}\,\mathrm{d}t \tag{1b}$$

$$\hat{u}_y(r,\theta,y,\omega) = \int_{-\infty}^{\infty} u_y(r,\theta,y,t)\mathrm{e}^{-\mathrm{i}\omega t}\,\mathrm{d}t \tag{1c}$$

where a hat above a variable denotes its representation in the frequency domain. A Fourier transform of the coordinate y to the wavenumber k_y is subsequently applied:

$$\breve{u}_r(r,\theta,k_y,\omega) = \int_{-\infty}^{\infty} \hat{u}_r(r,\theta,y,\omega)\mathrm{e}^{-\mathrm{i}k_y y}\,\mathrm{d}y \tag{2a}$$

$$\breve{u}_\theta(r,\theta,k_y,\omega) = \int_{-\infty}^{\infty} \hat{u}_\theta(r,\theta,y,\omega)\mathrm{e}^{-\mathrm{i}k_y y}\,\mathrm{d}y \tag{2b}$$

$$\breve{u}_y(r,\theta,k_y,\omega) = \int_{-\infty}^{\infty} \hat{u}_y(r,\theta,y,\omega)\mathrm{e}^{-\mathrm{i}k_y y}\,\mathrm{d}y \tag{2c}$$

where a breve above a variable denotes its representation in the frequency–wavenumber domain. Finally, a Fourier series expansion is employed in the circumferential direction:

$$\breve{u}_r(r,\theta,k_y,\omega) = \sum_{n=0}^{\infty} \tilde{u}_r(r,n,k_y,\omega)\,\cos(n\theta) \tag{3a}$$

$$\breve{u}_\theta(r,\theta,k_y,\omega) = \sum_{n=0}^{\infty} \tilde{u}_\theta(r,n,k_y,\omega)\,\sin(n\theta) \tag{3b}$$

$$\breve{u}_y(r,\theta,k_y,\omega) = \sum_{n=0}^{\infty} \tilde{u}_y(r,n,k_y,\omega)\,\cos(n\theta) \tag{3c}$$

where $\tilde{u}_r(r,n,k_y,\omega)$, $\tilde{u}_\theta(r,n,k_y,\omega)$, and $\tilde{u}_y(r,n,k_y,\omega)$ represent the frequency–wavenumber displacements for every harmonic component n in the Fourier series expansion. Since a vertical load F_z is applied at the tunnel invert, the resulting displacements are symmetric with respect to the (y,z)-plane. As a result, the displacements $\breve{u}_r(r,\theta,k_y,\omega)$ and $\breve{u}_y(r,\theta,k_y,\omega)$ are even functions of θ and a Fourier cosine series is used in Eqs. (3a) and (3c). The displacement $\breve{u}_\theta(r,\theta,k_y,\omega)$ is an odd function of θ and a Fourier sine series is used in Eq. (3b).

In a similar way, the stress components $\sigma_{rr}(r,\theta,y,t)$, $\sigma_{r\theta}(r,\theta,y,t)$, and $\sigma_{ry}(r,\theta,y,t)$ are transformed to the frequency–wavenumber domain. The stresses are subsequently decomposed using a Fourier series expansion in the circumferential direction:

$$\breve{\sigma}_{rr}(r,\theta,k_y,\omega) = \sum_{n=0}^{\infty} \tilde{\sigma}_{rr}(r,n,k_y,\omega)\,\cos(n\theta) \tag{4a}$$

$$\breve{\sigma}_{r\theta}(r,\theta,k_y,\omega) = \sum_{n=0}^{\infty} \tilde{\sigma}_{r\theta}(r,n,k_y,\omega)\,\sin(n\theta) \tag{4b}$$

$$\breve{\sigma}_{ry}(r,\theta,k_y,\omega) = \sum_{n=0}^{\infty} \tilde{\sigma}_{ry}(r,n,k_y,\omega)\,\cos(n\theta) \tag{4c}$$

Henceforth, all equations are derived in the frequency–wavenumber domain (r, n, k_y, ω). A summation for all harmonic components $n = 0, \ldots, n_{\max}$ (Eqs. (3) and (4)) and a double inverse Fourier transform finally results in the response in the space–time domain (r, θ, y, t).

The double Fourier transform to the frequency–wavenumber domain and the subsequent Fourier series expansion of the displacement and traction components allow for the analytical solution of wave propagation in the tunnel and the surrounding full space. Forrest and Hunt [6] employ wave potentials to demonstrate that the solution of elastic wave propagation can be written as

$$\tilde{\mathbf{u}}(r, n, k_y, \omega) = \tilde{\mathbf{U}}_r(r, n, k_y, \omega)\tilde{\mathbf{C}}(n, k_y, \omega) \tag{5}$$

and

$$\tilde{\boldsymbol{\sigma}}(r, n, k_y, \omega) = \tilde{\mathbf{T}}_r(r, n, k_y, \omega)\tilde{\mathbf{C}}(n, k_y, \omega) \tag{6}$$

where the vectors $\tilde{\mathbf{u}}(r, n, k_y, \omega) = \{\tilde{u}_r, \tilde{u}_\theta, \tilde{u}_y\}^{\mathrm{T}}$ and $\tilde{\boldsymbol{\sigma}}(r, n, k_y, \omega) = \{\tilde{\sigma}_{rr}, \tilde{\sigma}_{r\theta}, \tilde{\sigma}_{ry}\}^{\mathrm{T}}$ collect the radial, circumferential and longitudinal displacement and stress components, respectively. $\tilde{\mathbf{C}}(n, k_y, \omega)$ is a 6×1 vector of coefficients determined from the boundary conditions and $\tilde{\mathbf{U}}_r(r, n, k_y, \omega)$ and $\tilde{\mathbf{T}}_r(r, n, k_y, \omega)$ are the 3×6 displacement and stress matrices calculated at radius r, respectively. The elements of the first, the third and the fifth column of matrices $\tilde{\mathbf{U}}_r(r, n, k_y, \omega)$ and $\tilde{\mathbf{T}}_r(r, n, k_y, \omega)$ are a function of the modified Bessel function $I_n(r)$ of the first kind, while the elements of the second, the fourth and the sixth column are functions of the modified Bessel function $K_n(r)$ of the second kind. The matrices $\tilde{\mathbf{U}}_r(r, n, k_y, \omega)$ and $\tilde{\mathbf{T}}_r(r, n, k_y, \omega)$ are given in the closed form by Forrest and Hunt [6]. It should be noted that, in the original formulation, the longitudinal direction is along the z-axis instead of the y-axis.

Once the unknown vector of coefficients $\tilde{\mathbf{C}}(n, k_y, \omega)$ has been determined from the boundary conditions, the displacements $\tilde{\mathbf{u}}(r, n, k_y, \omega)$ and stresses $\tilde{\boldsymbol{\sigma}}(r, n, k_y, \omega)$ are found from Eqs. (5) and (6), respectively.

The displacement and stress solutions (5) and (6) are next used for the efficient solution of the 3D dynamic interaction between the tunnel and the full space. This requires the calculation of a coefficient vector $\tilde{\mathbf{C}}_T(n, k_y, \omega)$ for the tunnel and a coefficient vector $\tilde{\mathbf{C}}_F(n, k_y, \omega)$ for the full space, where the subscripts T and F refer to the tunnel and the full space, respectively (Fig. 3).

2.1.1. Wave propagation in the tunnel wall

The necessary equations to model a tunnel wall with internal radius r_i and external radius r_o are derived from Eqs. (5) and (6), which are directly applied at the internal radius r_i and the external radius r_o. This results in (Fig. 3b)

$$\tilde{\mathbf{u}}_{T1}(n, k_y, \omega) = \tilde{\mathbf{U}}_{T1}(n, k_y, \omega)\tilde{\mathbf{C}}_T(n, k_y, \omega) \tag{7}$$

and

$$\tilde{\boldsymbol{\tau}}_{T1}(n, k_y, \omega) = -\tilde{\mathbf{T}}_{T1}(n, k_y, \omega)\tilde{\mathbf{C}}_T(n, k_y, \omega) \tag{8}$$

on the tunnel wall $(r = r_i)$, and

$$\tilde{\mathbf{u}}_{T2}(n, k_y, \omega) = \tilde{\mathbf{U}}_{T2}(n, k_y, \omega)\tilde{\mathbf{C}}_T(n, k_y, \omega) \tag{9}$$

and

$$\tilde{\boldsymbol{\tau}}_{T2}(n, k_y, \omega) = \tilde{\mathbf{T}}_{T2}(n, k_y, \omega)\tilde{\mathbf{C}}_T(n, k_y, \omega) \tag{10}$$

on the tunnel–soil interface $(r = r_o)$, where $\tilde{\mathbf{u}}_{T1}$ and $\tilde{\mathbf{u}}_{T2}$ are the displacement vectors of the tunnel at the internal and external radii of the tunnel, respectively; $\tilde{\boldsymbol{\tau}}_{T1}$ and $\tilde{\boldsymbol{\tau}}_{T2}$ are the traction vectors calculated at the internal and external radii of the tunnel, respectively (Fig. 3b). The subscript T refers to the tunnel, subscript 1 to the internal radius of the tunnel and subscript 2 to the external radius. The minus sign in Eq. (8) originates from the negative orientation of the unit outward vector on the tunnel wall.

2.1.2. Wave propagation in a full space with a cylindrical cavity

Eqs. (5) and (6) are evaluated at $r = r_o$ (Fig. 3c):

$$\tilde{\mathbf{u}}_F(n, k_y, \omega) = \tilde{\mathbf{U}}_F(n, k_y, \omega)\tilde{\mathbf{C}}_F(n, k_y, \omega) \tag{11}$$

$$\tilde{\boldsymbol{\tau}}_F(n, k_y, \omega) = -\tilde{\mathbf{T}}_F(n, k_y, \omega)\tilde{\mathbf{C}}_F(n, k_y, \omega) \tag{12}$$

where $\tilde{\mathbf{u}}_F$ and $\tilde{\boldsymbol{\tau}}_F$ are the displacement and traction vectors in the full space at $r = r_o$ respectively. $\tilde{\mathbf{C}}_F$ is a 3×1 vector of constants. The subscript F is used to indicate values for the full space with a cylindrical cavity. The minus sign in Eq. (12) originates from the orientation of the unit outward normal vector on the surface of the cavity in the negative radial direction.

For a full space with a cylindrical cavity, the displacement should vanish at a large radius when the excitation source is applied at the surface of the cavity. These radiation conditions are accounted for by omitting the coefficients in the vector $\tilde{\mathbf{C}}_F$ associated with the modified Bessel function $I_n(r)$ of the first kind, since this function tends to infinity when its argument tends to infinity. As a result, the vector $\tilde{\mathbf{C}}_F$ is reduced to a 3×1 vector and the matrices $\tilde{\mathbf{U}}_F$ and $\tilde{\mathbf{T}}_F$ reduce to 3×3 matrices.

2.1.3. Solution of the coupled tunnel–soil interaction problem

The coefficient vectors $\tilde{\mathbf{C}}_T$ and $\tilde{\mathbf{C}}_F$ are determined from the boundary conditions on the tunnel wall at $r=r_i$ and the continuity of displacements and equilibrium of tractions at the tunnel–soil interface at $r=r_o$.

At the tunnel invert, a vertical point load F_z is applied whereas the rest of the tunnel wall remains traction free. This allows us to write the traction vector on the tunnel wall ($r=r_i$) as

$$\boldsymbol{\tau}_{T1}(\theta,y,t)=\left\{\begin{array}{c}0\\0\\\frac{\delta(\theta)\delta(t)}{r_i}\end{array}\right\} \tag{13}$$

The traction vector is subsequently transformed to the frequency–wavenumber domain and decomposed into harmonic components n:

$$\tilde{\boldsymbol{\tau}}_{T1}(n,k_y,\omega)=\left\{\begin{array}{c}0\\0\\\tilde{q}_r(n,k_y,\omega)\end{array}\right\} \tag{14}$$

where $\tilde{q}_r=1/(2\pi r_i)$ for $n=0$ and $\tilde{q}_r=1/(\pi r_i)$ for $n=1,2,\ldots,\infty$. At the tunnel–soil interface, displacement compatibility requires

$$\tilde{\mathbf{u}}_{T2}=\tilde{\mathbf{u}}_F \tag{15}$$

while the equilibrium of tractions reads as (Fig. 3c)

$$\tilde{\boldsymbol{\tau}}_{T2}+\tilde{\boldsymbol{\tau}}_F=\mathbf{0} \tag{16}$$

Eqs. (15) and (16) account for the 3D interaction between the tunnel and the full space. The boundary condition (14) at the tunnel wall, the continuity of displacements (15) and the equilibrium of forces (16) allow for the solution of the coefficient vectors $\tilde{\mathbf{C}}_T$ and $\tilde{\mathbf{C}}_F$ as the solution of Eqs. (8)–(12). Substituting the values of the displacement vectors $\tilde{\mathbf{u}}_{T2}$ and $\tilde{\mathbf{u}}_F$ from Eqs. (7) and (11) in Eq. (15) results in

$$\tilde{\mathbf{U}}_{T2}\tilde{\mathbf{C}}_T=\tilde{\mathbf{U}}_F\tilde{\mathbf{C}}_F \tag{17}$$

Similarly, substituting the values of the traction vectors $\tilde{\boldsymbol{\tau}}_{T2}$ and $\tilde{\boldsymbol{\tau}}_F$ from Eqs. (8) and (12) in Eq. (16) results in

$$\tilde{\mathbf{T}}_{T2}\tilde{\mathbf{C}}_T-\tilde{\mathbf{T}}_F\tilde{\mathbf{C}}_F=\mathbf{0} \tag{18}$$

Introducing Eq. (17) into Eq. (18) results in

$$(\tilde{\mathbf{T}}_{T2}-\tilde{\mathbf{T}}_F\tilde{\mathbf{U}}_F^{-1}\tilde{\mathbf{U}}_{T2})\tilde{\mathbf{C}}_T=\mathbf{0} \tag{19}$$

From Eqs. (8) and (19), the following expression is obtained:

$$\left[\begin{array}{c}-\tilde{\mathbf{T}}_{T1}\\\tilde{\mathbf{T}}_{T2}-\tilde{\mathbf{T}}_F\tilde{\mathbf{U}}_F^{-1}\tilde{\mathbf{U}}_{T2}\end{array}\right]\tilde{\mathbf{C}}_T=\left\{\begin{array}{c}\tilde{\boldsymbol{\tau}}_{T1}\\\mathbf{0}\end{array}\right\} \tag{20}$$

The vector $\tilde{\mathbf{C}}_T$ obtained from this equation is finally substituted in Eqs. (7) and (8) to obtain the displacement and the traction at the tunnel–soil interface for a tunnel embedded in a full space:

$$\tilde{\mathbf{u}}_{T2}=\tilde{\mathbf{U}}_{T2}\left[\begin{array}{c}-\tilde{\mathbf{T}}_{T1}\\\tilde{\mathbf{T}}_{T2}-\tilde{\mathbf{T}}_F\tilde{\mathbf{U}}_F^{-1}\tilde{\mathbf{U}}_{T2}\end{array}\right]^{-1}\left\{\begin{array}{c}\tilde{\boldsymbol{\tau}}_{T1}\\\mathbf{0}\end{array}\right\} \tag{21}$$

$$\tilde{\boldsymbol{\tau}}_{T2}=\tilde{\mathbf{T}}_{T2}\left[\begin{array}{c}-\tilde{\mathbf{T}}_{T1}\\\tilde{\mathbf{T}}_{T2}-\tilde{\mathbf{T}}_F\tilde{\mathbf{U}}_F^{-1}\tilde{\mathbf{U}}_{T2}\end{array}\right]^{-1}\left\{\begin{array}{c}\tilde{\boldsymbol{\tau}}_{T1}\\\mathbf{0}\end{array}\right\} \tag{22}$$

2.2. Step 2: calculating the equivalent loads

In the second calculation step, equivalent loads in a full space are determined that produce the same displacement at the tunnel–soil interface as calculated by the PiP model in the first calculation step.

The full space response is computed with the PiP model, where a solid cylinder with a radius r_o is coupled to a full space with a cylindrical cavity with radius r_o (Fig. 4).

The formulation presented in Section 2.1 is used to calculate the tractions $\tilde{\boldsymbol{\tau}}$ applied at the cylinder with $r=r_o$ in the full space, i.e. at the interface of the two sub-models, which produce the displacement $\tilde{\mathbf{u}}_{T2}$. This entails the calculation of coefficient vectors $\tilde{\mathbf{C}}_C$ and $\tilde{\mathbf{C}}_F$ for the cylinder and the full space, respectively, where the subscript C refers to the solid cylinder and the subscript F refers to the full space.

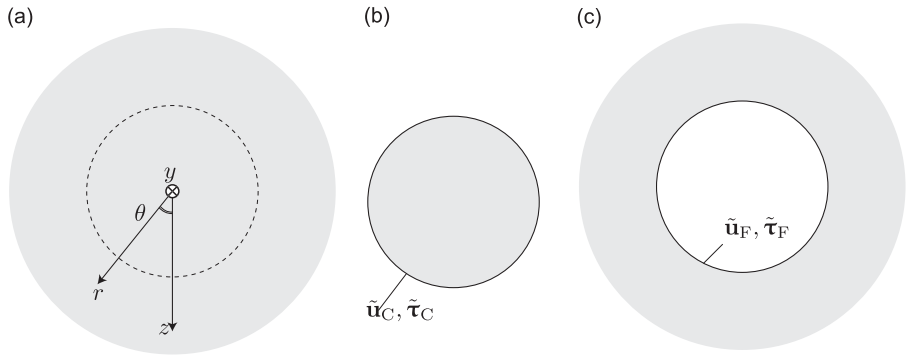

Fig. 4. Calculation step 2: (a) the full space response is computed as the dynamic interaction between (b) a solid cylinder and (c) a full space with a cylindrical cavity.

The displacement and the traction vector at the outer surface of the solid cylinder are derived from (Fig. 4b)

$$\tilde{\mathbf{u}}_C = \tilde{\mathbf{U}}_C \tilde{\mathbf{C}}_C \tag{23}$$

$$\tilde{\boldsymbol{\tau}}_C = \tilde{\mathbf{T}}_C \tilde{\mathbf{C}}_C \tag{24}$$

where $\tilde{\mathbf{C}}_C$ is a vector with (auxiliary) coefficients and $\tilde{\mathbf{U}}_C$ and $\tilde{\mathbf{T}}_C$ are the matrices derived from Eqs. (5) and (6), respectively.

The expressions for the displacement and the traction vector at the cavity surface are equal to (Fig. 4c)

$$\tilde{\mathbf{u}}_F = \tilde{\mathbf{U}}_F \mathbf{C}_F \tag{25}$$

$$\tilde{\boldsymbol{\tau}}_F = -\tilde{\mathbf{T}}_F \mathbf{C}_F \tag{26}$$

where $\tilde{\mathbf{C}}_F$ is a vector with (auxiliary) coefficients and $\tilde{\mathbf{U}}_F$ and $\tilde{\mathbf{T}}_F$ are the matrices derived from Eqs. (5) and (6), respectively. The minus sign in Eq. (26) originates from the orientation of the unit outward normal vector on the surface of the cavity in the negative radial direction.

Continuity of displacements at the interface between the solid cylinder and the surface of the cavity requires

$$\tilde{\mathbf{u}}_C = \tilde{\mathbf{u}}_F \tag{27}$$

Both displacement vectors are also equal to $\tilde{\mathbf{u}}_{T2}$, which allows us to express the vectors $\tilde{\mathbf{C}}_C$ and $\tilde{\mathbf{C}}_F$ as a function of the displacement vector $\tilde{\mathbf{u}}_{T2}$:

$$\tilde{\mathbf{C}}_C = \tilde{\mathbf{U}}_C^{-1} \tilde{\mathbf{u}}_{T2} \tag{28}$$

$$\tilde{\mathbf{C}}_F = \tilde{\mathbf{U}}_F^{-1} \tilde{\mathbf{u}}_{T2} \tag{29}$$

The traction vector $\tilde{\boldsymbol{\tau}}$ to be applied in the full space at the interface between the solid cylinder and the cavity surface in order to cause the displacement $\tilde{\mathbf{u}}_{T2}$ finally follows from the force equilibrium:

$$\tilde{\boldsymbol{\tau}} - \tilde{\boldsymbol{\tau}}_C - \tilde{\boldsymbol{\tau}}_F = 0 \tag{30}$$

Introduction of the expressions (24) and (26) and accounting for the solutions (28) and (29) result in the following expression:

$$\tilde{\boldsymbol{\tau}} = (\tilde{\mathbf{T}}_C \tilde{\mathbf{U}}_C^{-1} - \tilde{\mathbf{T}}_F \tilde{\mathbf{U}}_F^{-1}) \tilde{\mathbf{u}}_{T2} \tag{31}$$

Eq. (31) represents the equivalent traction, applied at a radius $r = r_o$ in a full space, that produces the same displacement on the tunnel–soil interface as computed in the first calculation step. A summation for all harmonic components $n = 0, \ldots, n_{\max}$ (Eqs. (3) and (4)) results in the traction $\check{\boldsymbol{\tau}}(\theta, k_y, \omega)$ in the frequency–wavenumber domain.

The tractions $\check{\boldsymbol{\tau}}(\theta, k_y, \omega)$ are next replaced by a set of equivalent loads $\check{\mathbf{F}}_j(k_y, \omega) = \{\check{F}_{rj}, \check{F}_{\theta j}, \check{F}_{yj}\}^{\mathrm{T}}$, applied at $2M-1$ points at the positions (r_o, θ_j) (Fig. 5). These equivalent loads are derived from the principle of virtual work, imposing that the virtual work of the tractions $\check{\boldsymbol{\tau}}(\theta, k_y, \omega)$ is equal to the virtual work of the equivalent loads $\check{\mathbf{F}}_j(k_y, \omega)$:

$$\int_0^{2\pi} \check{\mathbf{v}}^{\mathrm{T}}(\theta, k_y, \omega) \check{\boldsymbol{\tau}}(\theta, k_y, \omega)\, \mathrm{d}\theta = \sum_{j=1}^{2M-1} \check{\mathbf{v}}^{\mathrm{T}}(\theta_j, k_y, \omega) \check{\mathbf{F}}_j(k_y, \omega) \tag{32}$$

where $\check{\mathbf{v}}(\theta, k_y, \omega) = \{\check{v}_{rj}, \check{v}_{\theta j}, \check{v}_{yj}, \}^{\mathrm{T}}$ is a vector of virtual displacements on a circle with radius $r = r_o$. The virtual displacement vector is constructed from a linear shape function $N_j(\theta)$, as shown in Fig. 6. This allows us to compute the components of the

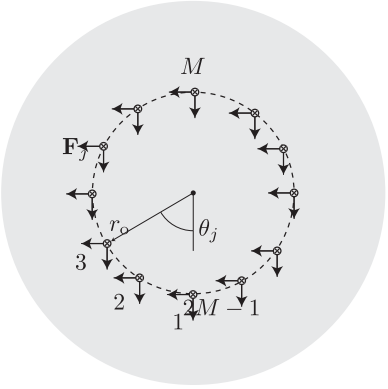

Fig. 5. Equivalent loads $\mathbf{F}_j$ $(j=1,\ldots,2M-1)$ applied at the position (r_o,θ_j).

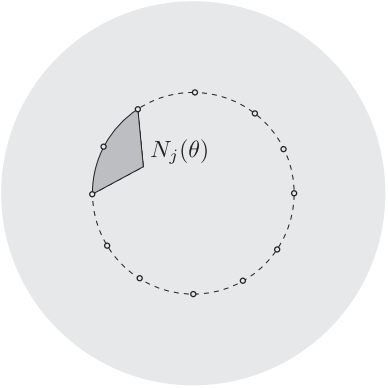

Fig. 6. Shape function $N(\theta_j)$.

equivalent loads $\check{\mathbf{F}}_j(k_y,\omega)$ as

$$\check{\mathbf{F}}_j(k_y,\omega)=\int_0^{2\pi} N_j(\theta)\check{\boldsymbol{\tau}}(\theta,k_y,\omega)\,\mathrm{d}\theta \tag{33}$$

Finally, the force vector $\check{\mathbf{F}}_j(k_y,\omega)=\{\check{F}_{rj},\check{F}_{\theta j},\check{F}_{yj}\}^{\mathrm{T}}$ is transformed to the Cartesian frame of reference, resulting in components $\check{F}_{xj}$, $\check{F}_{yj}$, and $\check{F}_{zj}$.

For the vertical loading under consideration, the distribution of equivalent loads is symmetric. Therefore, the evaluation of Eq. (33) can be limited to the loads on the left-hand side of the tunnel cross section ($j=1,\ldots,M$, Fig. 5) for computational efficiency. Symmetry conditions directly yield the forces on the right-hand side of the tunnel.

2.3. Step 3: calculating the far-field displacement

The equivalent loads $\check{\mathbf{F}}_j(k_y,\omega)=\{\check{F}_{xj},\check{F}_{yj},\check{F}_{zj}\}^{\mathrm{T}}$, resulting from the dynamic interaction between a tunnel and a homogeneous full space, are applied in calculation step 3 to a multi-layered half-space (Fig. 2c).

The response of the multi-layered half-space due to the set of equivalent loads $\check{\mathbf{F}}_j(k_y,\omega)=\{\check{F}_{xj},\check{F}_{yj},\check{F}_{zj}\}^{\mathrm{T}}$ is equal to

$$\check{u}_k(x,k_y,z,\omega)=\sum_{j=1}^{2M-1}\check{F}_{ij}(k_y,\omega)\check{u}_{ik}^{G}(x_j,z_j,x,k_y,z,\omega) \tag{34}$$

where $\check{u}_{ik}^{G}(x',z',x,k_y,z,\omega)$ is Green's displacement in the direction k due to an impulsive load applied in the direction i at the position (x',z') in the multi-layered half-space. Due to the invariance of the multi-layered half-space in the x-direction, a shift can be applied to both the source coordinate x' and the receiver coordinate x. This allows us to rewrite Eq. (34) as

$$\check{u}_k(x,k_y,z,\omega)=\sum_{j=1}^{2M-1}\check{F}_{ij}(k_y,\omega)\check{u}_{ik}^{G}(0,z_j,x-x_j,k_y,z,\omega) \tag{35}$$

Green's displacement $\check{u}_{ik}^{G}(x',z',x,k_y,z,\omega)$ for a multi-layered half-space is computed numerically by means of the direct stiffness method [24,25], since no closed form solutions are available [23]. In the direct stiffness method, the 3D Green's functions are commonly computed in a cylindrical coordinate system (r,θ,z). A semi-analytical solution is found after the

transformation of the radial coordinate r to the wavenumber k_r. More details on the solution of Green's function can be found in references [24,25].

Green's function can also be described in the Cartesian frame of reference (x,y,z); a transformation of the coordinates x and y to the wavenumbers k_x and k_y allows for a semi-analytical solution for Green's function $\check{\tilde{u}}_{ik}^{G}(z',k_x,k_y,z,\omega)$. More details on this approach can be found in references [17,18].

The latter approach is followed in this paper for the calculation of $\check{\tilde{u}}_{ik}^{G}(z',k_x,k_y,z,\omega)$. A Fourier transform from the coordinate x to the wavenumber k_x allows us to write Eq. (35) as

$$\check{\tilde{u}}_k(k_x,k_y,z,\omega)=\sum_{j=1}^{2M-1}\check{F}_{ij}(k_y,\omega)\check{\tilde{u}}_{ik}^{G}(z_j,k_x,k_y,z,\omega)e^{-\mathrm{i}k_x x_j} \tag{36}$$

As Green's functions $\check{\tilde{u}}_{ik}^{G}(z_j,k_x,k_y,z,\omega)$ are efficiently evaluated using the direct stiffness method, the evaluation of Eq. (36) directly yields the response $\check{\tilde{u}}_k(k_x,k_y,z,\omega)$ of the multi-layered half-space. A triple inverse Fourier transform results in the displacement $u_k(x,y,z,t)$.

3. Case histories

In order to assess the applicability of the proposed method, five cases are selected (Fig. 7). In all cases, the tunnel has an inner radius $r_i=2.75$ m and an outer radius $r_o=3.0$ m and is made of concrete with Young's modulus $E=50$ GPa, Poisson's ratio $\nu=0.3$ and a density $\rho=2500$ kg/m^3. Attenuation is introduced through a loss factor $\eta=0.03$ associated with both Lamé constants.

Case 1 (Fig. 7a) is the reference case of a tunnel embedded in a full space with a shear wave velocity $C_s=200$ m/s, a dilatational wave velocity $C_p=400$ m/s, a density $\rho=1800$ kg/m^3, and a loss factor $\eta=0.04$ associated with both Lamé constants.

Case 2 (Fig. 7b) corresponds to a tunnel embedded in a homogeneous half-space, with the same properties as the full space in case 1. The depth D_e of the tunnel is varied from 5 to 20 m (Table 1). For a depth $D_e=5$ m (case 2a), it can be expected that reflected waves at the free surface influence the tunnel wall displacements. For larger depths (e.g. $D_e=20$ m, case 2c), reflected waves are expected to have a minor influence.

In case 3 (Fig. 7c), a tunnel embedded in a layered half-space is considered. The layered half-space consists of a soft layer on top of a homogeneous half-space. The properties of the half-space are the same as in case 1. The soft layer has a shear wave velocity $C_s=100$ m/s, a dilatational wave velocity $C_p=200$ m/s, a density $\rho=1800$ kg/m^3, and a loss factor $\eta=0.04$ associated with both Lamé constants. The corresponding stiffness contrast between the layer and the half-space equals 4, which is large. The tunnel depth is fixed to 20 m and the thickness of the soft layer is varied according to the values in

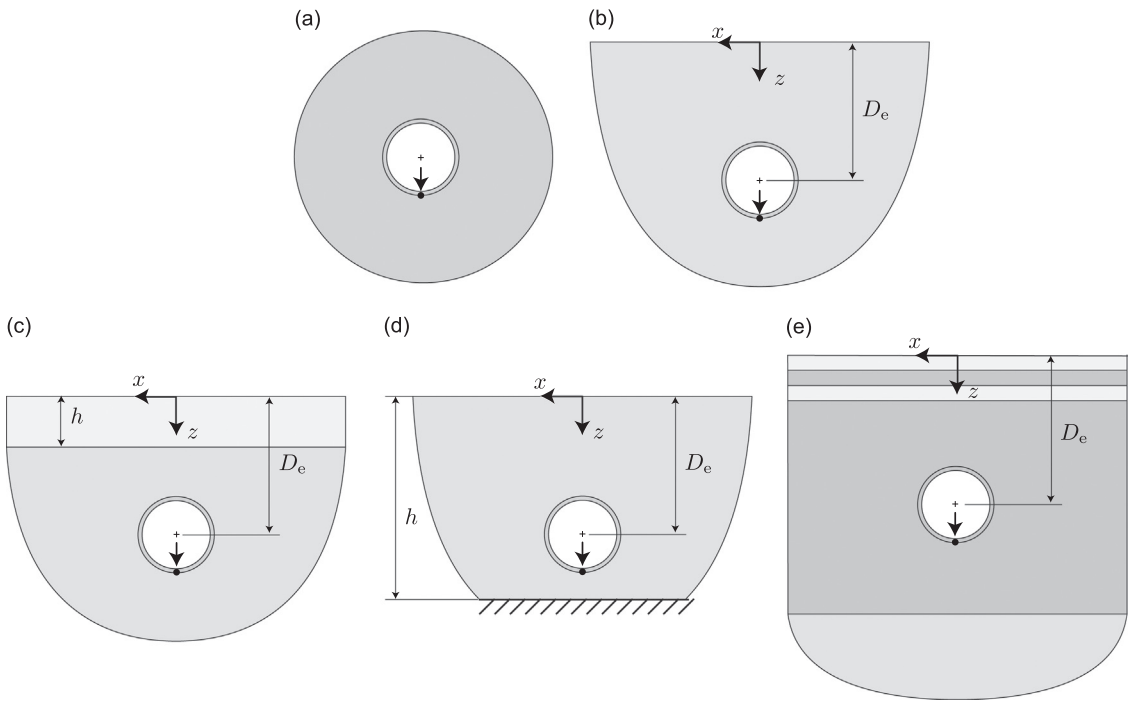

Fig. 7. Tunnel embedded in (a) a full space (case 1), (b) a homogeneous half-space (case 2), (c) a layered half-space (case 3), (d) a layer on bedrock (case 4) and (e) a layered half-space (case 5).

Table 1
Tunnel depth and layer geometry used in the case study.

Case	Depth D_e (m)	Layer thickness h (m)
2a	5	–
2b	10	–
2c	20	–
3a	20	5
3b	20	10
3c	20	20
4a	20	25
4b	20	30
4c	20	50
5	20	–

Table 2
Soil layering for case 5.

Layer thickness (m)	C_s (m/s)	C_p (m/s)	ρ (kg/m^3)
1	50	100	1100
3	100	200	1500
1	50	100	1100
20	200	400	1800
∞	300	600	1800

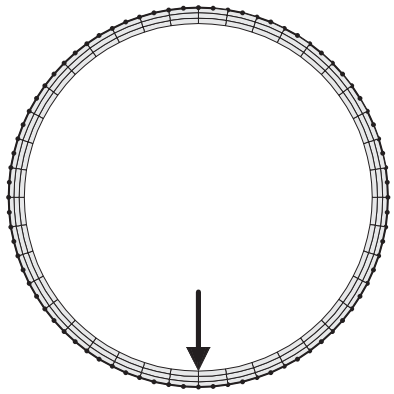

Fig. 8. 2.5D finite element mesh of the tunnel used in the coupled FE–BE calculations.

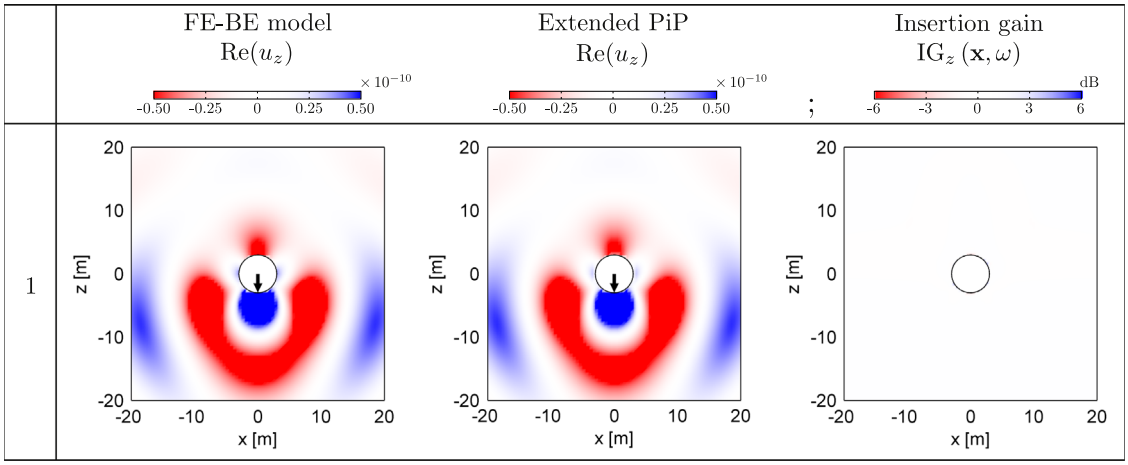

Fig. 9. Real part of the vertical displacement in the soil for case 1 at 10 Hz, as computed with the coupled FE–BE model (left) and the extended PiP model (center). The insertion gain $\mathrm{IG}_z(\mathbf{x}, \omega)$ between both solutions is also plotted (right).

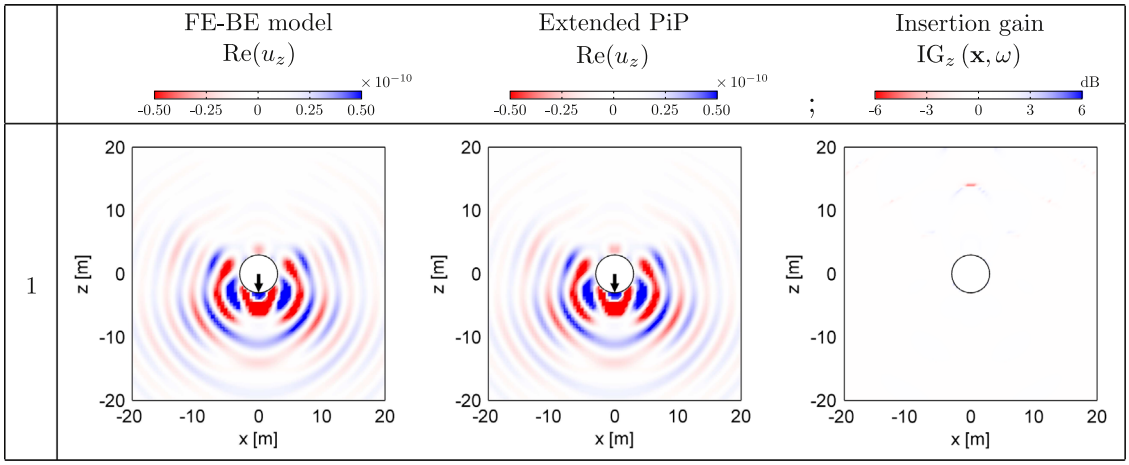

Fig. 10. Real part of the vertical displacement in the soil for case 1 at 50 Hz, as computed with the coupled FE–BE model (left) and the extended PiP model (center). The insertion gain $IG_z(\mathbf{x}, \omega)$ between both solutions is also plotted (right).

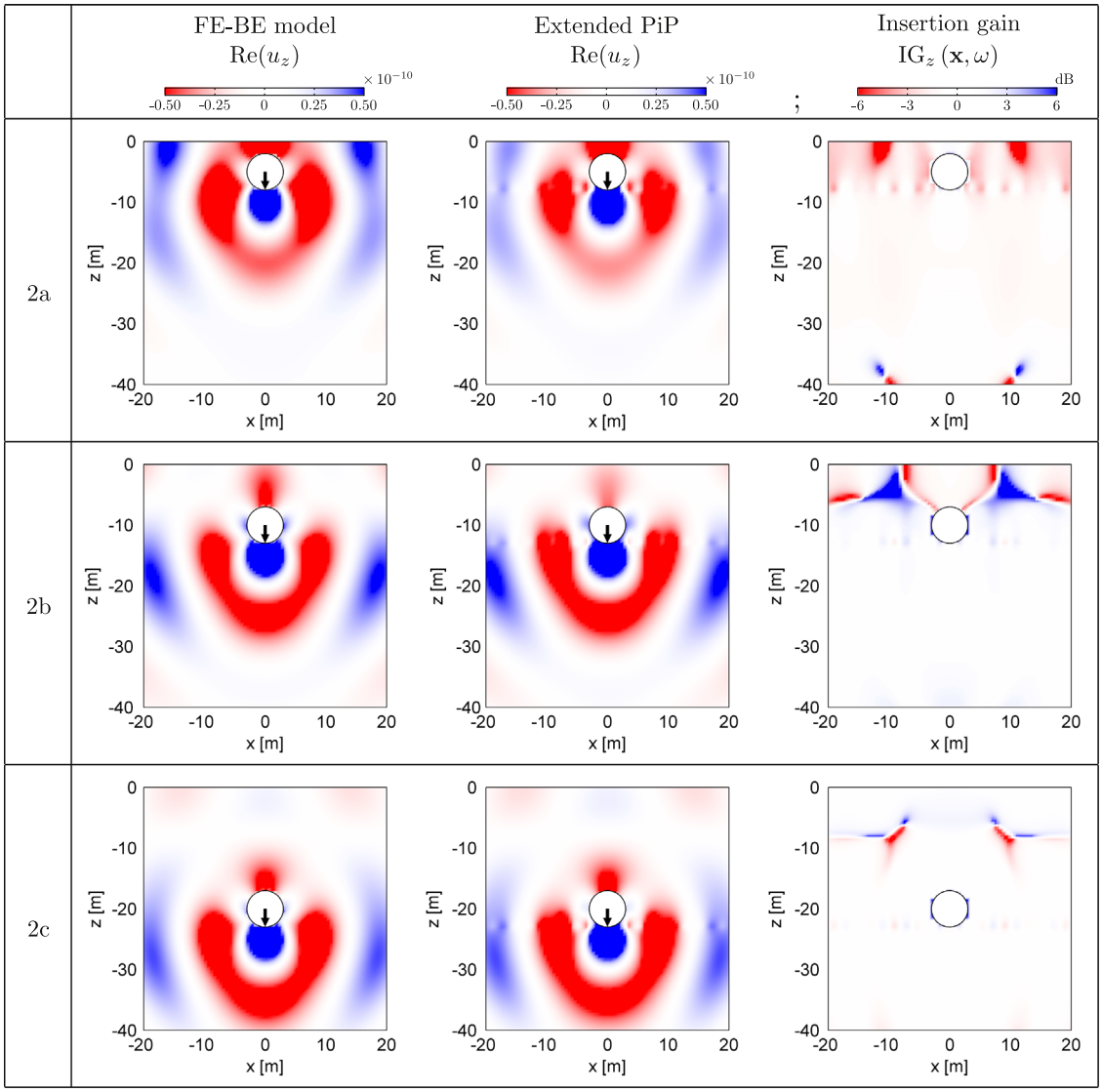

Fig. 11. Real part of the vertical displacement in the soil for cases 2a, 2b, and 2c at 10 Hz, as computed with the coupled FE–BE model (left) and the extended PiP model (center). The insertion gain $IG_z(\mathbf{x}, \omega)$ between both solutions is also plotted (right).

Table 1. In the case where the depth D_e is equal to the layer thickness h, the interface between the soil layer and the half-space intersects the tunnel, which is expected to importantly affect the tunnel response. At a small layer thickness (e.g. $h=5$ m, case 3a) the effect of waves reflected on the interface is expected to have a small influence on the tunnel response.

In case 4 (Fig. 7d), a tunnel embedded in a layer on a bedrock is considered. The soil layer has the same properties as the soil in case 1. The tunnel depth is fixed to 20 m and the soil layer thickness is varied from 25 to 50 m (Table 1). In case 4a, the distance between the bedrock and the tunnel invert equals 2.125 m and it is expected that the wave reflected on the bedrock influences the tunnel wall displacements. At larger layer thicknesses (e.g. $h=50$ m, case 4c), the reflected waves are expected to have a minor influence.

In case 5, the tunnel is embedded in a multi-layered half-space with soft top layers (Table 2). The soil layering is inspired by soil conditions prevailing in the Groene Hart region in the Netherlands, where the Groene Hart tunnel has been constructed [15]. The site is characterized by peat and clay inclusions with underlying sand layers. The tunnel depth is fixed to 20 m.

The response of the tunnel and the soil due to a harmonic point load at the tunnel invert is computed in the frequency range between 1 and 80 Hz with a step of 1 Hz. All results are calculated first in the wavenumber domain using the methodology described in the previous section. The results are subsequently transformed to the spatial domain using a double inverse discrete Fourier transform. The results of the PiP model are calculated using a personal computer with 1 GB RAM and 2.4 GHz processor.

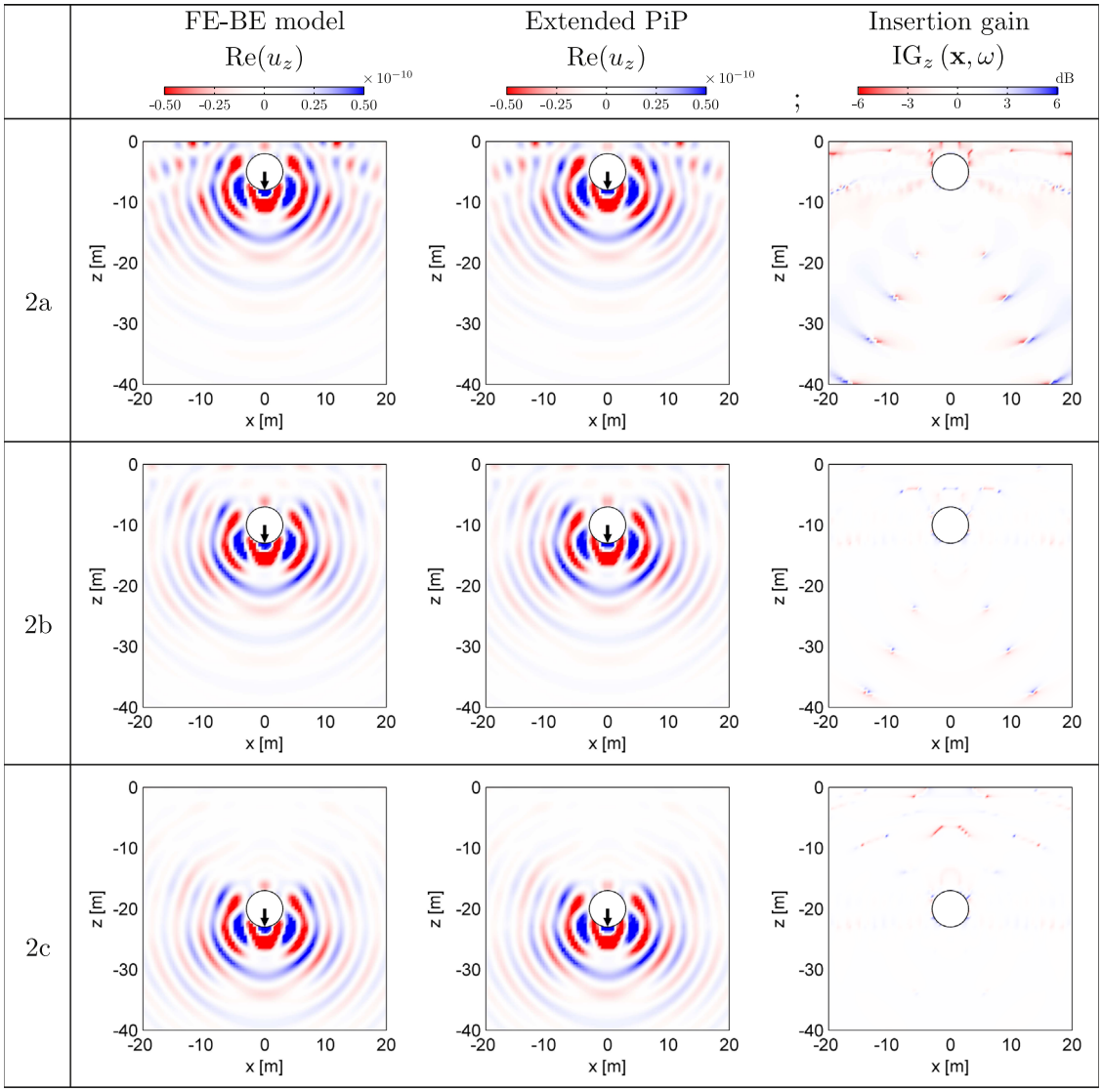

Fig. 12. Real part of the vertical displacement in the soil for cases 2a, 2b, and 2c at 50 Hz, as computed with the coupled FE–BE model (left) and the extended PiP model (center). The insertion gain IG$_z(\mathbf{x}, \omega)$ between both solutions is also plotted (right).

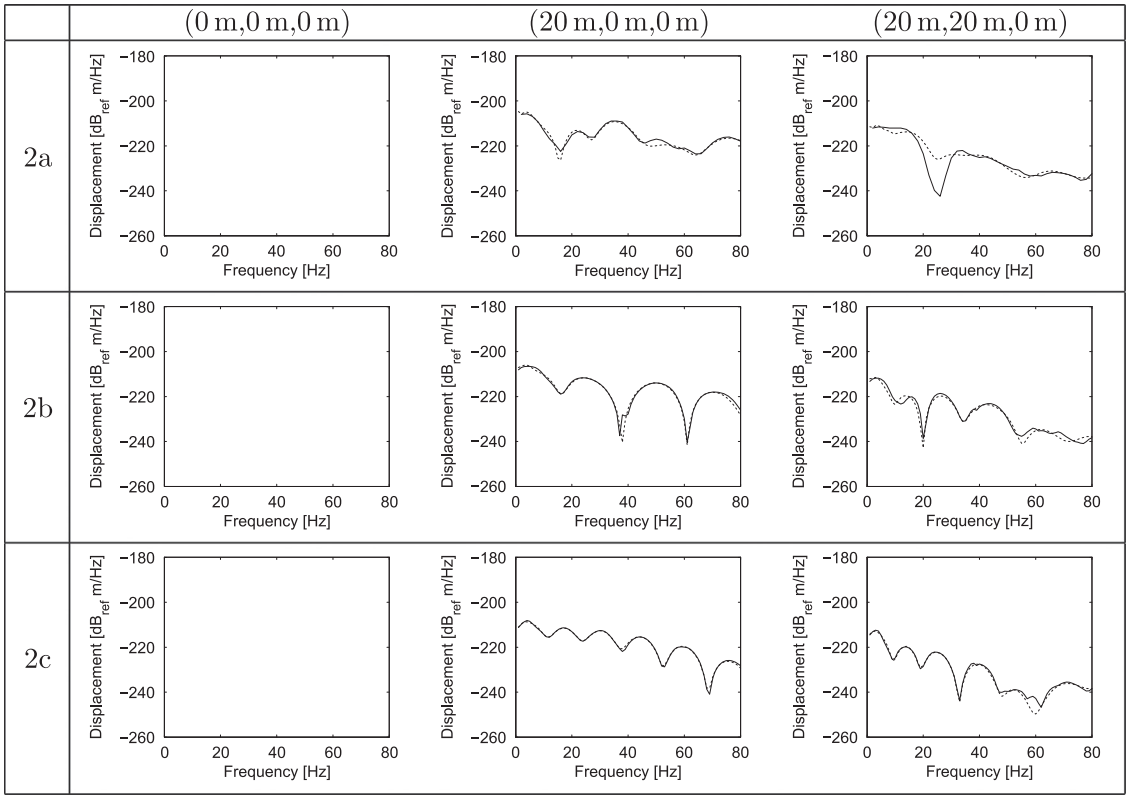

Fig. 13. Modulus of the displacement $\hat{u}_x$ in three points (0 m, 0 m, 0 m), (20 m, 0 m, 0 m), and (20 m, 20 m, 0 m) on the free surface for cases 2a, 2b, and 2c, as computed with the coupled FE–BE model (solid line) and the extended PiP model (dashed line). It should be noted that, at the point (0 m, 0 m, 0 m), the displacement component $\hat{u}_x$ is equal to zero as a result of symmetry.

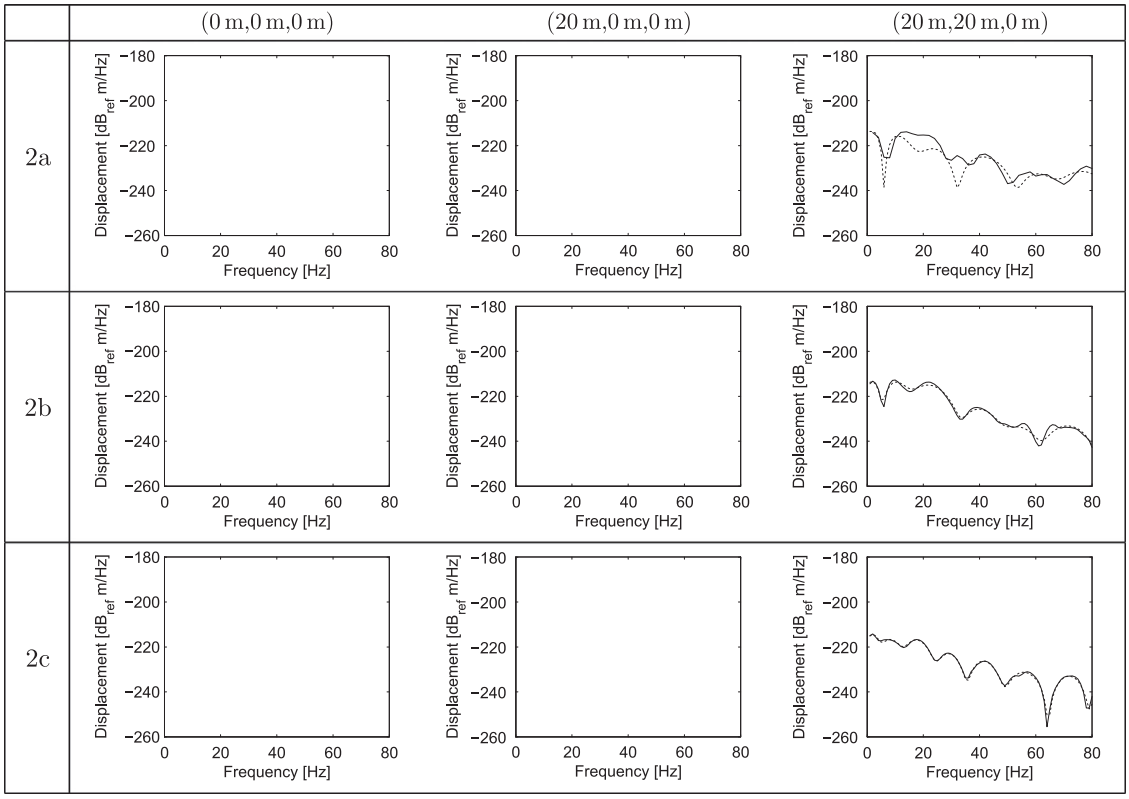

Fig. 14. Modulus of the displacement $\hat{u}_y$ in three points (0 m, 0 m, 0 m), (20 m, 0 m, 0 m), and (20 m, 20 m, 0 m) on the free surface for cases 2a, 2b, and 2c, as computed with the coupled FE–BE model (solid line) and the extended PiP model (dashed line). It should be noted that, at the points (0 m, 0 m, 0 m) and (20 m, 0 m, 0 m), the displacement component $\hat{u}_y$ is equal to zero as a result of symmetry.

The results are compared with the results obtained with a fully coupled 2.5D FE–BE model [18]. The 2.5D finite element mesh consists of a regular mesh of 120 8-node serendipity elements (Fig. 8). The boundary element mesh conforms with the finite element mesh and consists of 40 quadratic node-collocated elements of equal size. The boundary integral equation is integrated using 6 Gaussian integration points per element.

The FE–BE results are calculated using a single hexa-core Xeon 5650 Westmere 2.66 GHz CPU processor of the high performance cluster at KU Leuven. Frequencies higher than 80 Hz are not considered due to the high computational cost of the FE–BE model as a result of the finer mesh required. The considered frequency range is of practical interest for ground-borne vibration in buildings and is sufficient for the validation of the models developed in this work.

The computation time for the problem under consideration for each frequency and wavenumber is about 5 s for the extended PiP calculation and about 100 s for the coupled FE–BE calculation. The high computational cost of the coupled FE–BE model is related to the calculation of the tunnel response, where source locations of Green's functions are considered at every boundary element node. The computational advantage of the extended PiP model results from the use of an approximate solution of the tunnel response. For the computation of the radiated wavefield in the soil from the tunnel response, there is no significant gain in computation time between both methods. Regarding memory requirements, both models require less than 1 GB of RAM. This is related to the use of a 2.5D model, where the 2D FE and BE meshes have a limited amount of degrees of freedom.

3.1. Case 1: reference case of a tunnel embedded in a full space

In order to verify the correctness of the implementation, the vertical displacement in the soil for case 1 of a tunnel embedded in a full space is first computed using both the coupled FE–BE model and the extended PiP model. In the extended PiP model, equivalent loads are computed that produce the same displacement at the tunnel–soil interface. The analytical full space Green's functions [17] are subsequently used to compute the radiated wavefield. Figs. 9 and 10 show the resulting vertical displacement in the soil at 10 Hz and 50 Hz, respectively, as computed with both methods. As expected, a very good correspondence is observed.

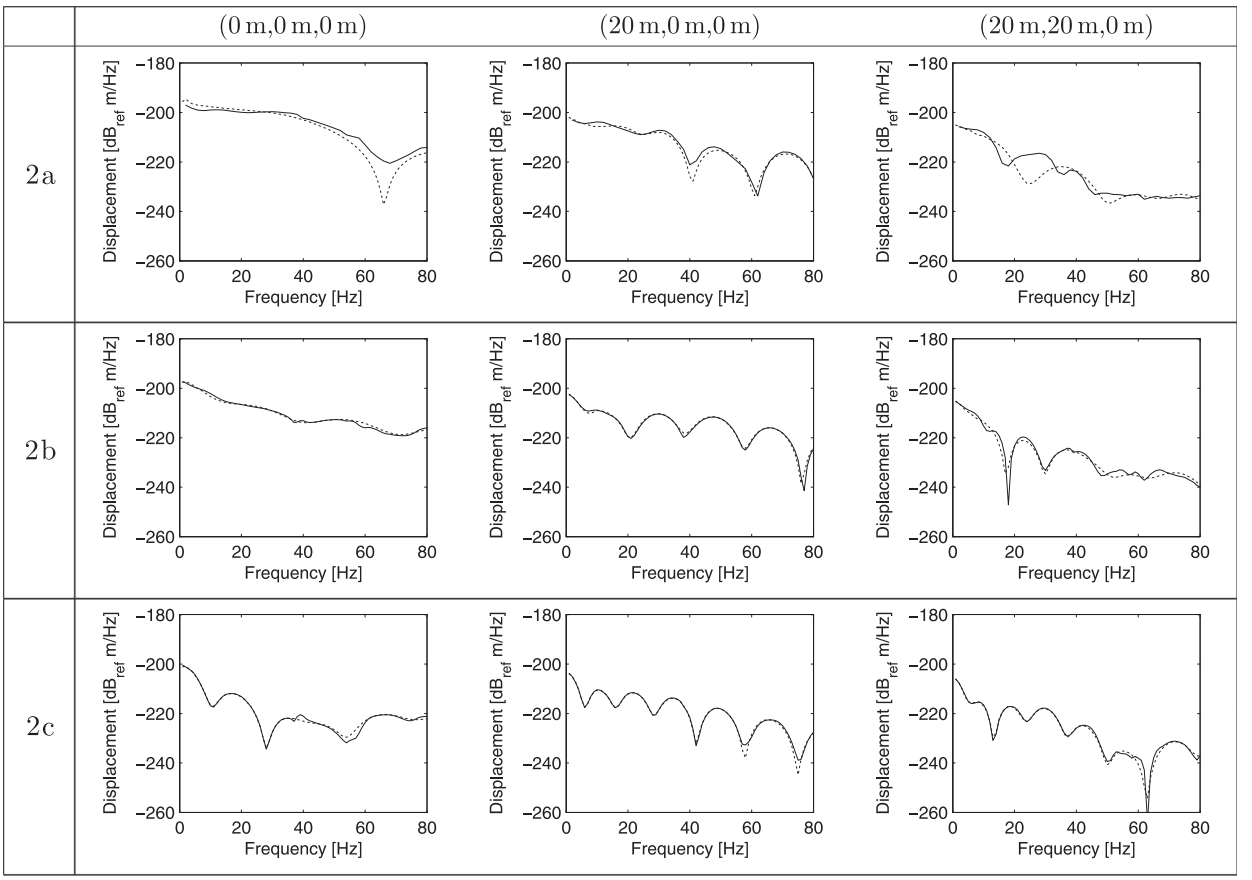

Fig. 15. Modulus of the displacement $\hat{u}_z$ in three points (0 m, 0 m, 0 m), (20 m, 0 m, 0 m), and (20 m, 20 m, 0 m) on the free surface for cases 2a, 2b, and 2c, as computed with the coupled FE–BE model (solid line) and the extended PiP model (dashed line).

In order to further compare both solution methods, the insertion gain between both solutions is computed as

$$\mathrm{IG}_z(\mathbf{x},\omega) = 20\log_{10}\left(\frac{|u_z(\mathbf{x},\omega)|}{|u_z^0(\mathbf{x},\omega)|}\right) \tag{37}$$

where $|u_z^0(\mathbf{x},\omega)|$ is the reference solution computed with the fully coupled FE–BE model and $|u_z(\mathbf{x},\omega)|$ is the solution obtained with the extended PiP model.

Figs. 9 and 10 show the insertion gain at 10 Hz and 50 Hz, respectively, demonstrating that, for the full space solution, the insertion gain $\mathrm{IG}_z(\mathbf{x},\omega)$ remains negligible at 10 Hz, while a small error is observed at 50 Hz. This is attributed to the different discretization methods used for the computation of the radiated wavefield. In the coupled FE–BE model, the integral representation theorem is applied over the soil–tunnel interface [18] while the extended PiP model uses equivalent loads. The difference between both solutions remains small, however, and can be further reduced by considering a higher number of boundary elements in the coupled FE–BE model and equivalent loads in the extended PiP model.

3.2. Case 2: tunnel embedded in a homogeneous half-space

In case 2, a tunnel embedded in a homogeneous half-space is considered where the tunnel depth is varied from 5 to 20 m. Figs. 11 and 12 show the wavefield in cases 2a, 2b and 2c as computed with the fully coupled FE–BE model and with

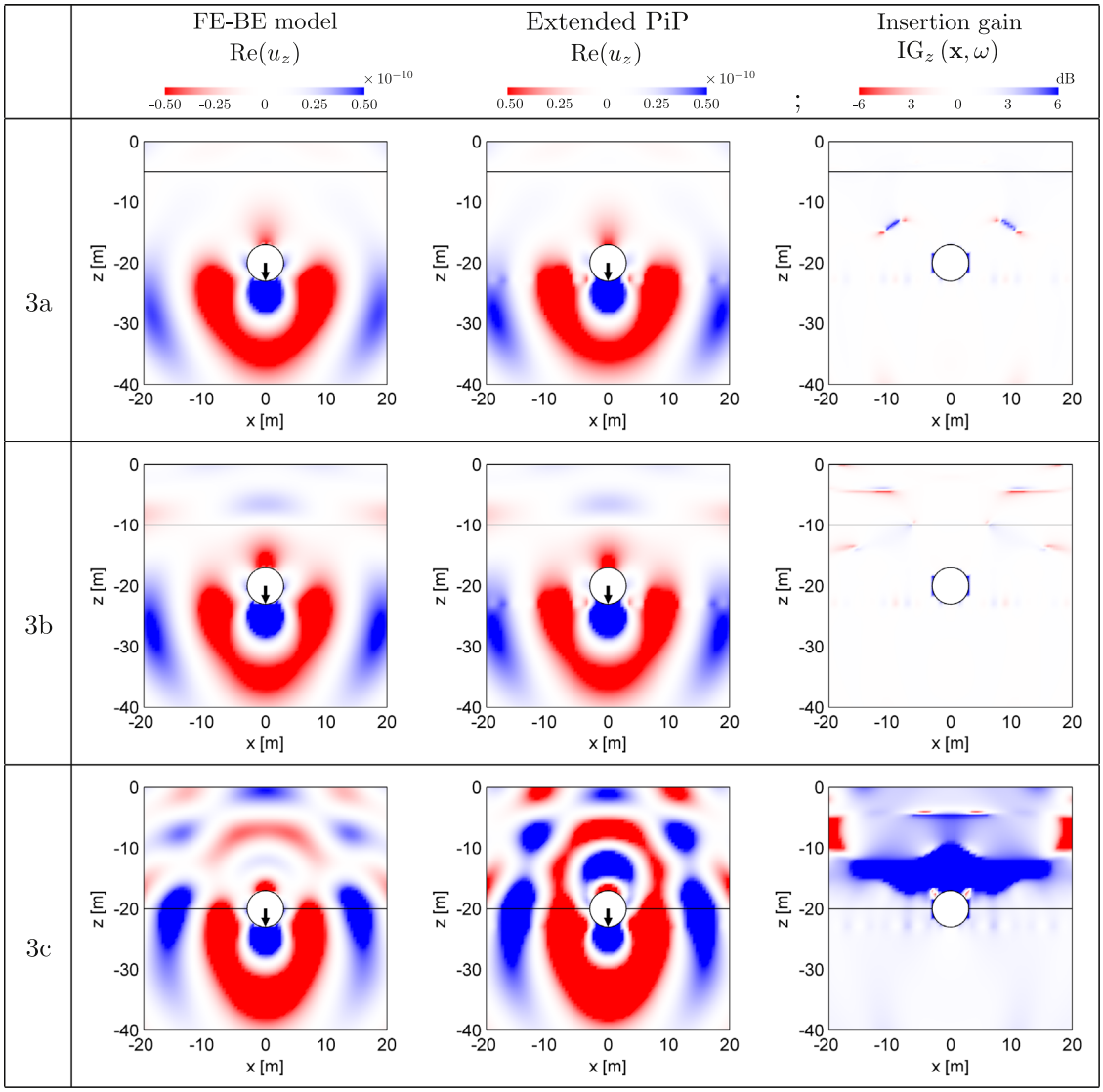

Fig. 16. Real part of the vertical displacement in the soil for cases 3a, 3b, and 3c at 10 Hz, as computed with the coupled FE–BE model (left) and the extended PiP model (center). The insertion gain $\mathrm{IG}_z(\mathbf{x},\omega)$ between both solutions is also plotted (right).

the extended PiP model at 10 Hz and 50 Hz, respectively. For a tunnel depth of 5 m (case 2a), the wavefield computed with the extended PiP model deviates from the reference solution, as a result of the influence of the free surface on the tunnel response. Visual comparison of the wave fields allows, however, us to conclude that the extended PiP model results in a good qualitative prediction of the soil response.

The insertion gain is also plotted in Figs. 11 and 12. The insertion gain is small below the load point in cases 2b and 2c, whereas significant differences are observed above the tunnel in all cases. However, the insertion gain plots should be interpreted with care, due to the presence of zones of constructive and destructive interference, resulting from the superposition of direct waves and waves reflected at the free surface. A small spatial shift of the interference pattern may therefore result in a large insertion gain. This is specifically true at higher frequencies, where smaller wavelengths result in a closer spacing of the zones of constructive and destructive interference. This is apparent in the insertion gain plots for all cases 2a, 2b, and 2c (Figs. 11 and 12): the large insertion gain corresponds to a large relative error, but this is due to small

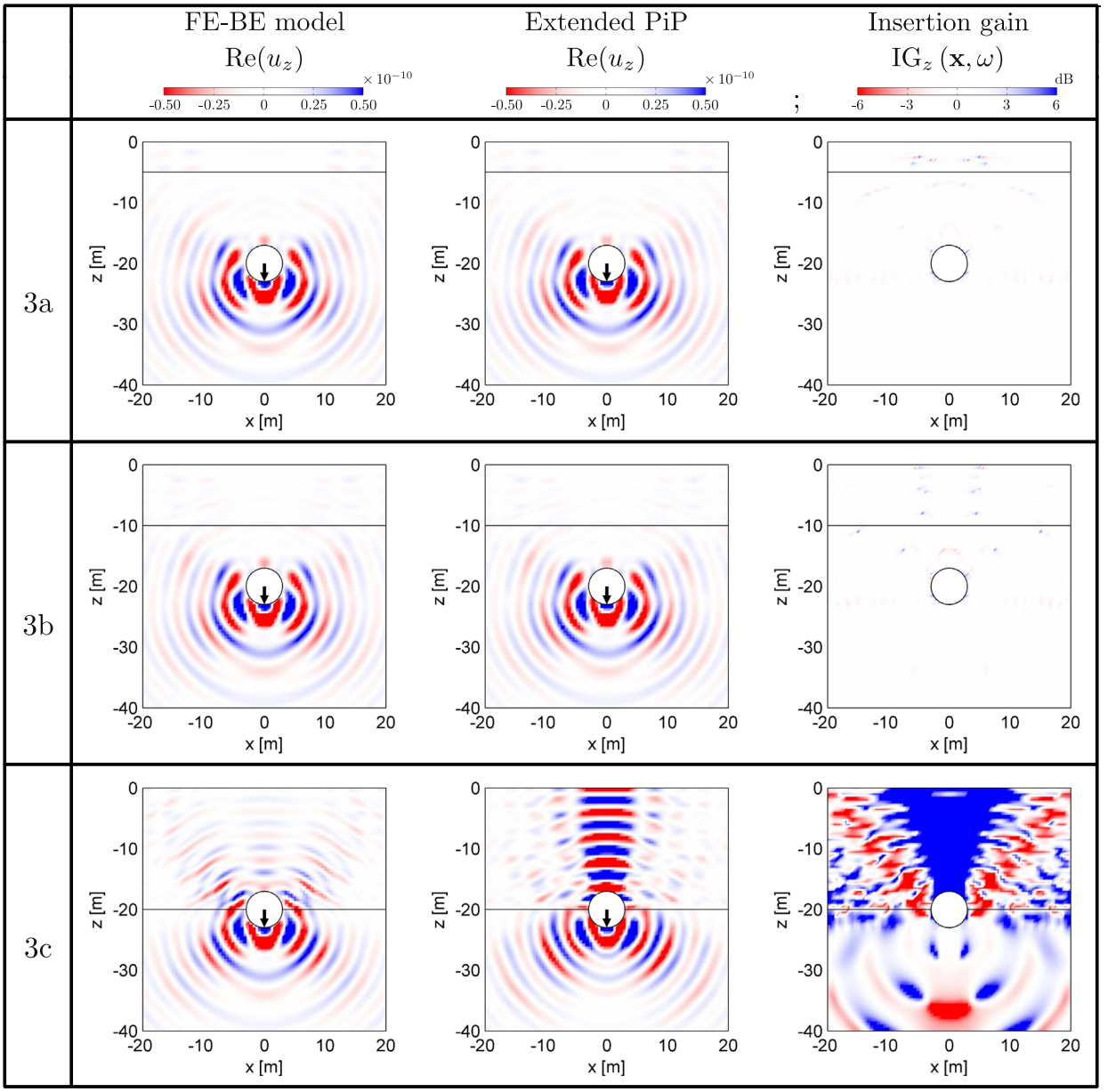

Fig. 17. Real part of the vertical displacement in the soil for cases 3a, 3b, and 3c at 50 Hz, as computed with the coupled FE–BE model (left) and the extended PiP model (center). The insertion gain IG$_z(\mathbf{x}, \omega)$ between both solutions is also plotted (right).

spatial shifts of the interference pattern. Accounting for these effects, it can be concluded that both solutions are in good agreement, especially for cases 2b and 2c with a large tunnel depth.

The displacements at the free surface are important for engineering practice, since vibrations at ground surface are frequently used in the assessment of underground train induced vibrations and vibration countermeasures in the track structure. Figs. 13–15 show the modulus of the three displacement components in three points (0 m, 0 m, 0 m), (20 m, 0 m, 0 m), and (20 m, 20 m, 0 m) on the free surface for cases 2a, 2b, and 2c, as computed with the coupled FE–BE model and the extended PiP model. It should be noted that, at the point (0 m, 0 m, 0 m), the displacement components $\hat{u}_x$ and $\hat{u}_y$ are equal to zero as a result of symmetry. Similarly, at the point (20 m, 0 m, 0 m) the displacement component $\hat{u}_y$ equals zero.

For case 2a, a difference between both solutions is observed as a result of the reflection of waves at the free surface. The displacements are not accurately computed, but still acceptable for environmental vibration studies in an early design stage. For cases 2b and 2c, the accuracy of the PiP approach is very good.

3.3. Case 3: tunnel embedded in a layered half-space

In case 3, a tunnel embedded in a layered half-space is considered. The layered half-space consists of a soft layer on top of a homogeneous half-space where the layer thickness is varied from 5 to 20 m. Figs. 16 and 17 show the wavefield as computed with the fully coupled FE–BE model and the extended PiP model at 10 Hz and 50 Hz, respectively.

A visual comparison of the wave fields allows to conclude that the extended PiP model results in a good qualitative prediction of the soil response for cases 3a and 3b. At both frequencies, the wave patterns in the soft top layer are similar, but spatial shifts of the interference pattern result in large insertion gains. This demonstrates that the PiP model is of practical use as a scoping tool in an early design stage.

In case 3c, the interface between the soft soil layer and the half-space intersects the tunnel. The response of the stiff underlying half-space is well predicted by the extended PiP model, whereas a large error is made in the soft top layer. This is explained as follows. In the case of the extended PiP calculation, the tunnel displacement corresponds to the case of the tunnel embedded in a full space with the same properties as the half-space (case 1). This allows to correctly compute the response of the bottom half of the tunnel wall, whereas the response of the top half of the tunnel wall is overestimated.

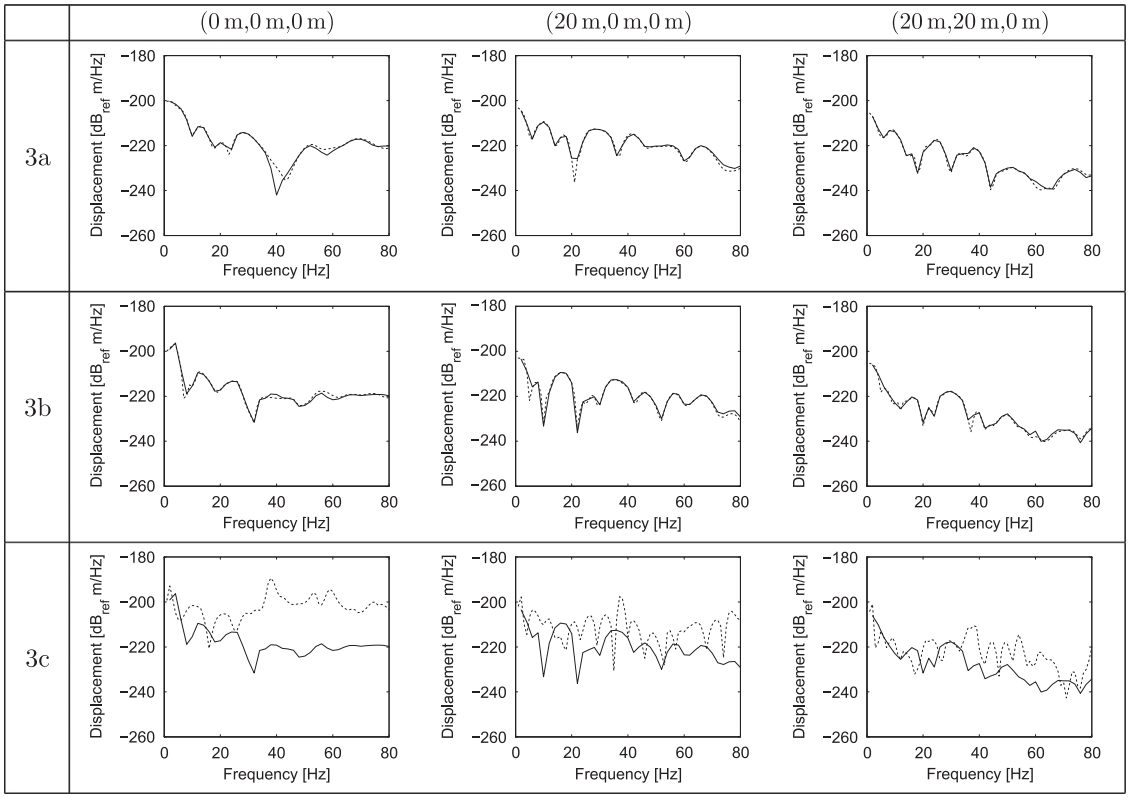

Fig. 18. Modulus of the displacement $\hat{u}_z$ in three points at (0 m, 0 m, 0 m), (20 m, 0 m, 0 m), and (20 m, 20 m, 0 m) on the free surface for cases 3a, 3b, and 3c, as computed with the coupled FE–BE model (solid line) and the extended PiP model (dashed line).

In the case of the coupled FE–BE model, the tunnel imposes its stiffness to the soft top soil layer that results in a smaller response.

One could alternatively consider the properties of the soft layer (or an average value) for the calculation of the tunnel response in the extended PiP calculation. This would result, however, in an overestimation of the overall response. For the present case where the tunnel intersects a layer interface, the dynamic interaction between the tunnel and the multi-layered half-space is clearly different from the assumption made in calculation step 1 of the PiP model.

The present case demonstrates that an accurate solution can be obtained at all frequencies if the distance between the tunnel and the free surface or the layer interface is larger than one or two times the tunnel diameter. This distance should not be interpreted in terms of number of wavelengths, since the tunnel and the near field soil (quasi-static) response predominantly depend on the soil properties near the tunnel.

Fig. 18 shows the modulus of the vertical displacement in three points (0 m, 0 m, 0 m), (20 m, 0 m, 0 m), and (20 m, 20 m, 0 m) on the free surface for cases 3a, 3b, and 3c, as computed with the coupled FE–BE model and the extended PiP model. A similar observation is made as in case 2 : if the tunnel and the layer interface are sufficiently spaced, the correspondence between both methods is very good. Under these conditions, the extended PiP model can be used as an accurate tool for environmental vibration studies in an early design stage. In case 3c, a large error is observed, in correspondence with Figs. 16 and 17.

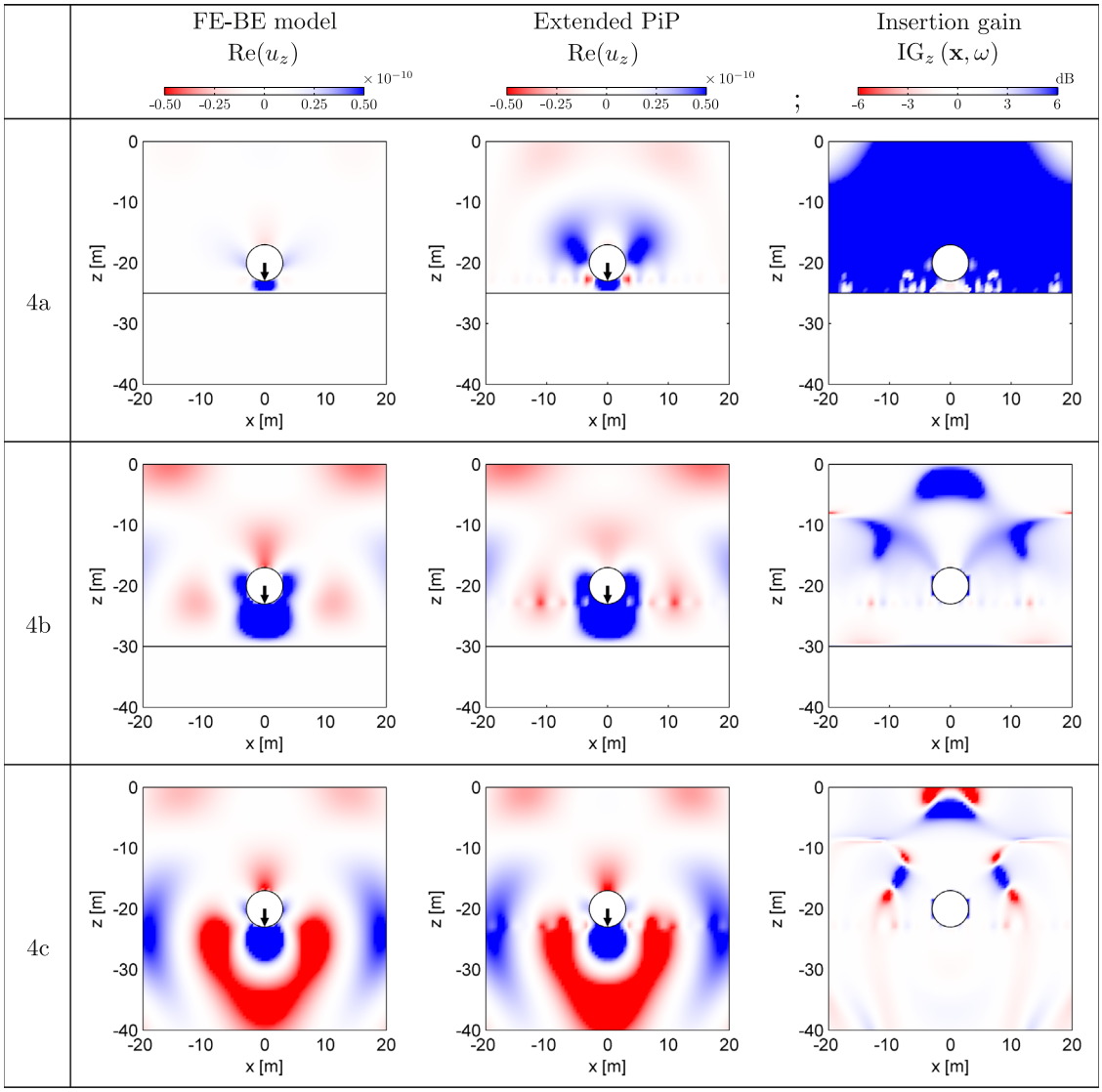

Fig. 19. Real part of the vertical displacement in the soil for cases 4a, 4b, and 4c at 10 Hz, as computed with the coupled FE–BE model (left) and the extended PiP model (center). The insertion gain $IG_z(\mathbf{x}, \omega)$ between both solutions is also plotted (right).

3.4. Case 4: tunnel embedded in a layer on a bedrock

In case 4, a tunnel embedded in a layer on a bedrock is considered where the layer thickness is varied from 25 to 50 m. Figs. 19 and 20 show the wavefield in cases 4a, 4b and 4c as computed with the fully coupled FE–BE model and with the extended PiP model at 10 Hz and 50 Hz, respectively.

In case 4a, the distance between the tunnel and the bedrock is small, resulting in an increased soil impedance at the bottom of the tunnel at 10 Hz. Accordingly, this results in a limited vertical displacement of the load point and an overall reduction of response of the tunnel and the soil with respect to case 1. The extended PiP calculation overestimates the tunnel response and the amplitude of the radiated wavefield. At 50 Hz, this effect is less pronounced and the resulting wavefields computed with the fully coupled FE–BE model and the extended PiP approach are compared well. However, spatial shifts of the interference pattern, resulting from the superposition of direct waves and waves reflected at the free surface and the bedrock, can be observed. The insertion gain plots should therefore be interpreted with care. A similar observation can be made for cases 4b and 4c at both 10 Hz and 50 Hz. Both solutions are in agreement, apart from small spatial shifts in the interference pattern.

Fig. 21 shows the modulus of the vertical displacement in three points (0 m, 0 m, 0 m), (20 m, 0 m, 0 m), and (20 m, 20 m, 0 m) on the free surface. For case 4a, the extended PiP calculation overestimates the tunnel response due to the close

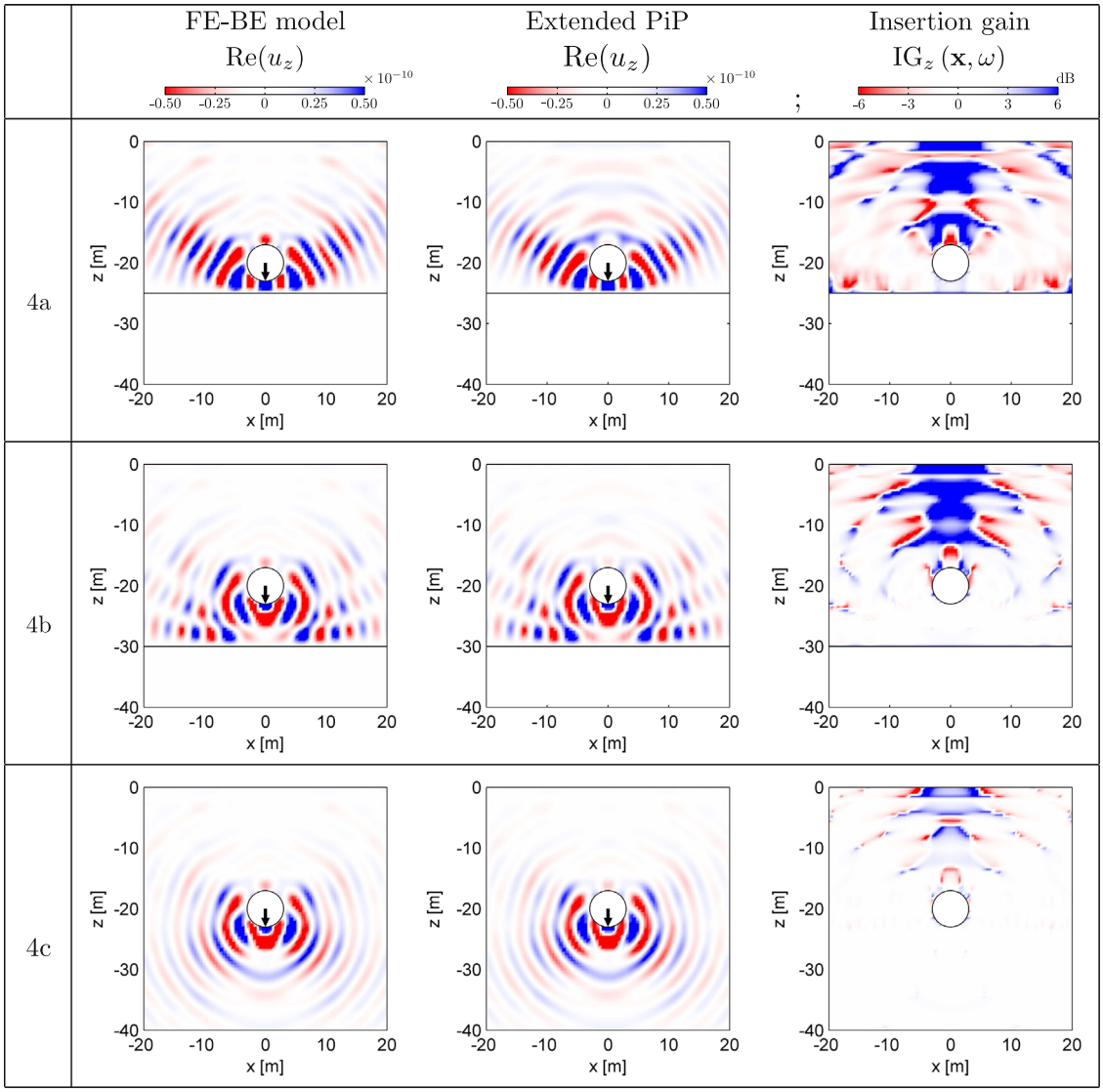

Fig. 20. Real part of the vertical displacement in the soil for cases 4a, 4b, and 4c at 50 Hz, as computed with the coupled FE–BE model (left) and the extended PiP model (center). The insertion gain $\mathrm{IG}_z(\mathbf{x},\omega)$ between both solutions is also plotted (right).

distance between the tunnel and the bedrock. This further results in a large overestimation of the free field displacements in all three points considered.

For the cases 4b and 4c, the correspondence is good between both solutions. However, the difference is larger than in the previous cases 2 and 3, since the bedrock is located below the tunnel, which has a larger effect on the dynamic tunnel–soil interaction. However, the accuracy of the extended PiP model is still acceptable for environmental vibration studies.

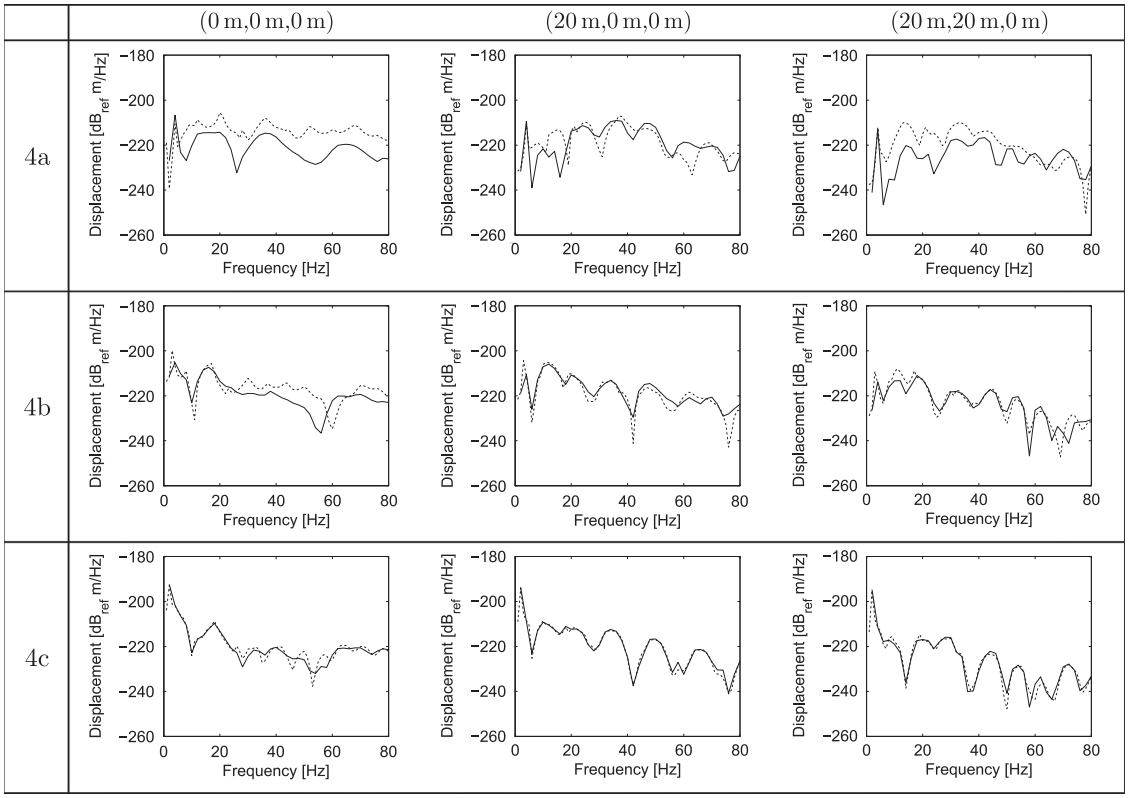

Fig. 21. Modulus of the displacement $\hat{u}_z$ in three points at (0 m, 0 m, 0 m), (20 m, 0 m, 0 m), and (20 m, 20 m, 0 m) on the free surface for cases 4a, 4b, and 4c, as computed with the coupled FE–BE model (solid line) and the extended PiP model (dashed line).

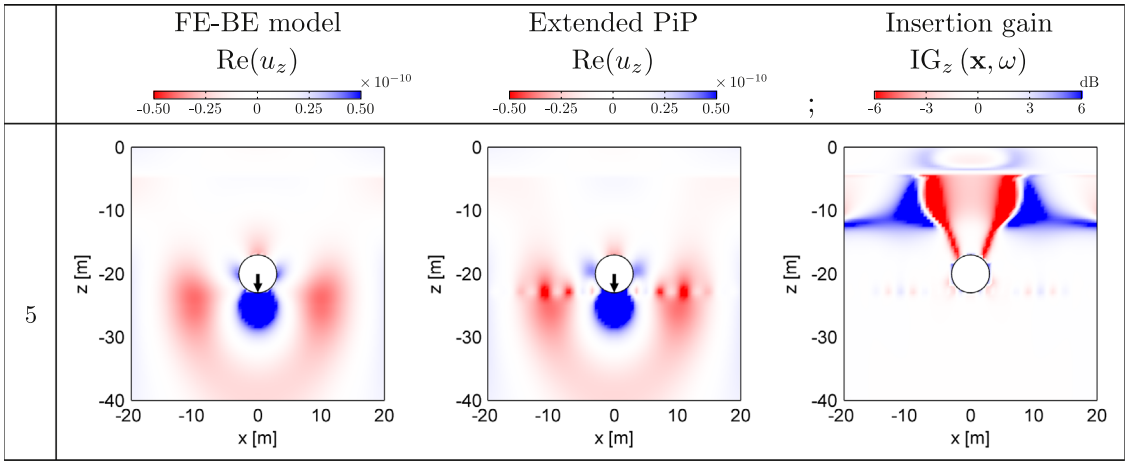

Fig. 22. Real part of the vertical displacement in the soil for case 5 at 10 Hz, as computed with the coupled FE–BE model (left) and the extended PiP model (center). The insertion gain $IG_z(\mathbf{x}, \omega)$ between both solutions is also plotted (right).

3.5. Case 5: tunnel embedded in a multi-layered half-space

In case 5, the tunnel is embedded in a multilayered half-space characterized by soft top layers (Table 2). Figs. 22 and 23 show the wavefield as computed with the fully coupled FE–BE model and with the extended PiP model at 10 Hz and 50 Hz, respectively.

A visual comparison of the wave fields allows to conclude that the extended PiP model results in a good qualitative prediction of the soil response. At both frequencies, the wave patterns in the soft top layer are similar, but spatial shifts of the interference pattern result in large insertion gains.

Fig. 24 shows the modulus of the vertical displacement in three points (0 m, 0 m, 0 m), (20 m, 0 m, 0 m), and (20 m, 20 m, 0 m) on the free surface. A similar observation is made as in the previous cases: since the distance between the tunnel and the layer interfaces is sufficiently large, the correspondence between both methods is very good. Under these

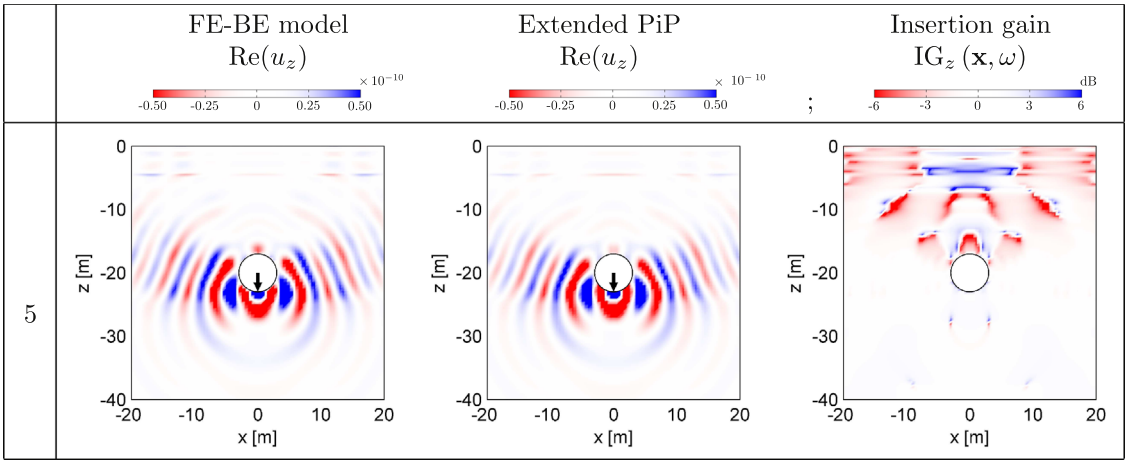

Fig. 23. Real part of the vertical displacement in the soil for case 5 at 50 Hz, as computed with the coupled FE–BE model (left) and the extended PiP model (center). The insertion gain $IG_z(\mathbf{x}, \omega)$ between both solutions is also plotted (right).

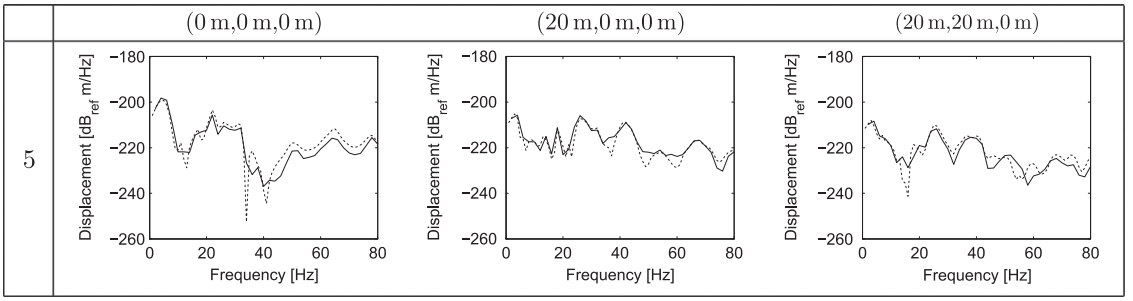

Fig. 24. Modulus of the displacement $\hat{u}_z$ in three points at (0 m, 0 m, 0 m), (20 m, 0 m, 0 m), and (20 m, 20 m, 0 m) on the free surface for case 5, as computed with the coupled FE–BE model (solid line) and the extended PiP model (dashed line).

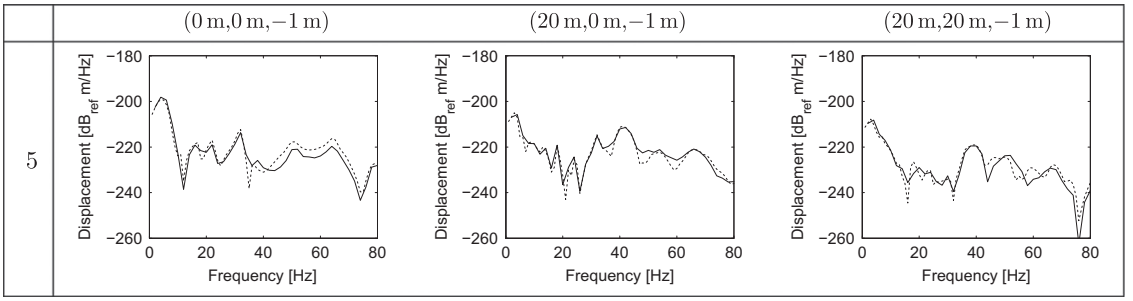

Fig. 25. Modulus of the displacement $\hat{u}_z$ in three points at (0 m, 0 m, −2 m), (20 m, 0 m, −2 m), and (20 m, 20 m, −2 m) for case 5, as computed with the coupled FE–BE model (solid line) and the extended PiP model (dashed line).

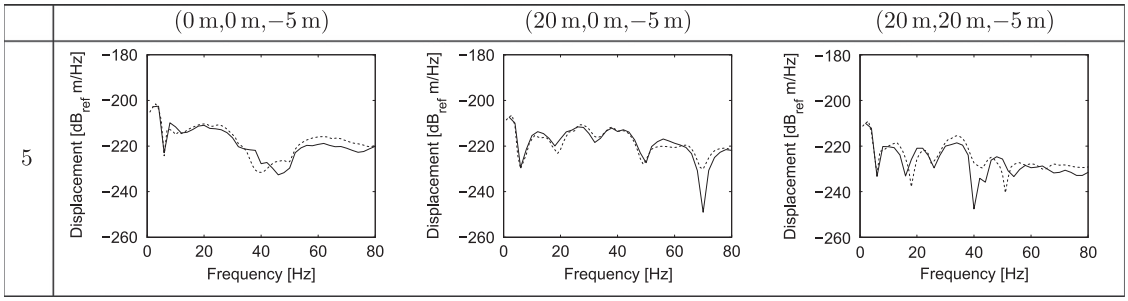

Fig. 26. Modulus of the displacement $\hat{u}_z$ in three points at (0 m, 0 m, −5 m), (20 m, 0 m, −5 m), and (20 m, 20 m, −5 m) for case 5, as computed with the coupled FE–BE model (solid line) and the extended PiP model (dashed line).

conditions, the extended PiP model can be used as an accurate design tool. This also holds in the present case of a complicated soil layering where wave propagation is governed by strong reflections on layer interfaces.

Figs. 25 and 26 show the modulus of the vertical displacement in three points on the interface between soil layers at a depth of 1 m and 5 m, respectively. The difference between both models is comparable to the results at the free surface. This is due to the fact that the radiation of waves in calculation step 3 fully accounts for wave propagation in the layered soil.

4. Conclusion

The previous study demonstrates that the extended PiP model allows to accurately predict the response of the multi-layered half-space. While spatial shifts of the interference pattern resulting from the superposition of direct waves and waves reflected at the free surface and the bedrock can be observed, the overall response of the multi-layered half-space is well predicted in most cases. Therefore, the extended PiP model provides a computationally efficient design tool to predict vibration from underground tunnels in an early design phase. The extended PiP model is also applicable to assess the performance of vibration countermeasures, such as under sleeper pads or a floating slab track.

If the distance between the tunnel and the free surface or the layer interface is small, the accuracy deteriorates, but is still acceptable. As a general rule, a good solution is obtained if the distance between the tunnel and the free surface or layer interface is not larger than two times the tunnel diameter.

Acknowledgment

The second author is a Postdoctoral Fellow of the Research Foundation – Flanders (FWO). The support of FWO is gratefully acknowledged.

References

[1] C.J.C. Jones, J.R. Block, Prediction of ground vibration from freight trains, *Journal of Sound and Vibration* 193 (1) (1996) 205–213.
[2] P. Grootenhuis, Floating track slab isolation for railway, *Journal of Sound and Vibration* 51 (3) (1977) 443–448.
[3] J.T. Nelson, Recent developments in ground-borne noise and vibration control, *Journal of Sound and Vibration* 193 (1) (1996) 367–376.
[4] P.J. Remington, L.G. Kurzweil, D.A. Towers, Low-frequency noise and vibration from trains, in: P. Nelson (Ed.), *Transportation Noise*, 1987 (Chapter 16).
[5] G.P. Wilson, H.J. Saurenman, J.T. Nelson, Control of ground-borne noise and vibration, *Journal of Sound and Vibration* 87 (2) (1983) 339–350.
[6] J.A. Forrest, H.E.M. Hunt, A three-dimensional tunnel model for calculation of train-induced ground vibration, *Journal of Sound and Vibration* 294 (2006) 678–705.
[7] J.A. Forrest, H.E.M. Hunt, Ground vibration generated by trains in underground tunnels, *Journal of Sound and Vibration* 294 (2006) 706–736.
[8] M.F.M. Hussein, H.E.M. Hunt, A numerical model for calculating vibration from a railway tunnel embedded in a full-space, *Journal of Sound and Vibration* 305 (2007) 401–431.
[9] X. Sheng, C.J.C. Jones, D.J. Thompson, Prediction of ground vibration from trains using the wavenumber finite and boundary element methods, *Journal of Sound and Vibration* 293 (2006) 575–586.
[10] D. Clouteau, M. Arnst, T.M. Al-Hussaini, G. Degrande, Freefield vibrations due to dynamic loading on a tunnel embedded in a stratified medium, *Journal of Sound and Vibration* 283 (1–2) (2005) 173–199.
[11] G. Degrande, D. Clouteau, R. Othman, M. Arnst, H. Chebli, R. Klein, P. Chatterjee, B. Janssens, A numerical model for ground-borne vibrations from underground railway traffic based on a periodic finite element-boundary element formulation, *Journal of Sound and Vibration* 293 (3–5) (2006) 645–666.
[12] H. Chebli, R. Othman, D. Clouteau, M. Arnst, G. Degrande, 3D periodic BE-FE model for various transportation structures interacting with soil, *Computers and Geotechnics* 35 (2008) 22–32.
[13] S. Gupta, M.F.M. Hussein, G. Degrande, H.E.M. Hunt, D. Clouteau, A comparison of two numerical models for the prediction of vibrations from underground railway traffic, *Soil Dynamics and Earthquake Engineering* 27 (7) (2007) 608–624.
[14] S. Gupta, G. Degrande, G. Lombaert, Experimental validation of a numerical model for subway induced vibrations, *Journal of Sound and Vibration* 321 (3–5) (2009) 786–812.
[15] S. Gupta, H. Van den Berghe, G. Lombaert, G. Degrande, Numerical modelling of vibrations from a Thalys high speed train in the Groene Hart tunnel, *Soil Dynamics and Earthquake Engineering* 30 (2010) 82–97.
[16] D. Aubry, D. Clouteau, G. Bonnet, Modelling of wave propagation due to fixed or mobile dynamic sources, in: N. Chouw, G. Schmid (Eds.), *Workshop Wave* '94, *Wave propagation and Reduction of Vibrations*, Ruhr Universität Bochum, Germany, December 1994, pp. 109–121.

[17] A.J.B. Tadeu, E. Kausel, Green's functions for two-and-a-half-dimensional elastodynamic problems, *ASCE Journal of Engineering Mechanics* 126 (10) (2000) 1093–1096.
[18] S. François, M. Schevenels, G. Lombaert, P. Galvín, G. Degrande, A 2.5D coupled FE–BE methodology for the dynamic interaction between longitudinally invariant structures and a layered halfspace, *Computer Methods in Applied Mechanics and Engineering* 199 (23–24) (2010) 1536–1548.
[19] H. Grundmann, K. Muller, Dynamic interaction of a plate elastically mounted on a tunnel, in: Proceedings of the Sixth European Conference on Structural Dynamics, EURODYN, Paris, France, 2005, pp. 1273–1278.
[20] K. Müller, H. Grundmann, S. Lenz, Nonlinear interaction between a moving vehicle and a plate elastically mounted on a tunnel, *Journal of Sound and Vibration* 310 (2008) 558–586.
[21] V.A. Babeshko, M.G. Seleznev, T.N. Selezneva, V.P. Sokolov, On a method of studying steady-state oscillations of an elastic half-space containing a cavity, *Applied Mathematics and Mechanics* 47 (1) (1983) 88–93. (English translation of Prikladnaya Matematika i Mekhanika).
[22] G.E. Kolodyazhnaya, M.G. Seleznev, T.N. Selezneva, Problem of a uniformly moving oscillating load acting on an elastic half-space containing a recessed cylindrical cavity, *Mechanics of Solids* 22 (6) (1987) 83–87. (English translation of Izvestiya Akademii Nauk SSSR, Mekhanika Tverdogo Tela).
[23] E. Kausel, *Fundamental Solutions in Elastodynamics: A Compendium*, Cambridge University Press, New York, 2006.
[24] E. Kausel, J.M. Roësset, Stiffness matrices for layered soils, *Bulletin of the Seismological Society of America* 71 (6) (1981) 1743–1761.
[25] M. Schevenels, S. François, G. Degrande, EDT: *an ElastoDynamics Toolbox for MATLAB*, *Computers & Geosciences* 35 (8) (2009) 1752–1754.